1

Chemistry of Pentazole

Ming Lu, Pengcheng Wang, Yuangang Xu, and Qiuhan Lin

Nanjing University of Science and Technology, School of Chemistry and Chemical Engineering, Xiaolingwei 200#, Nanjing, 210094, PR China

1.1 Introduction

The pentazolate anion, usually referred to as "*cyclo*-N_5^-," is an all-nitrogen-containing five-membered-ring compound that has recently attracted significant levels of attention; *cyclo*-N_5^- represents an important member of the azole ring family and is an isoelectronic nitrogen analogue of the cyclopentadienide anion [1, 2]. Furthermore, the decomposition of *cyclo*-N_5^- into dinitrogen (N_2) and N_3^- is exothermic by 14.3 kcal mol^{-1}, while the activation energy for this decomposition is 27.2 kcal mol^{-1}. The heat of formation, ΔH_f (298 K, N_5^-), is 59.6 kcal mol^{-1} [3–5], while the vertical ionization energy of *cyclo*-N_5^-, which refers to the formation of neutral N_5 while maintaining the geometry of *cyclo*-N_5^-, has been calculated to be 5.6 eV [5]. These data indicate that *cyclo*-N_5^- is very likely to exist after isolation, potentially becoming the next polynitrogen species in the field of energetic materials. The unique properties of the *cyclo*-N_5^- ring have motivated extensive efforts toward exploring this unknown structure by synthetic chemists [4, 6].

1.2 Substituted Pentazoles

The exploration of *cyclo*-N_5^- has been a difficult and time-consuming process [7]. Experimental progress stagnated at the substituted pentazole stage for a long period of time because the aromaticity of the *cyclo*-N_5 ring is strongly affected and even broken through the attachment of substituents. Consequently, substituted pentazoles are too sensitive for use under most laboratory conditions, and researchers have to investigate them by in-depth computational studies, including the stabilities, as well as the formation and decomposition mechanisms. Here, we classify substituted pentazoles according to their substituted groups.

Nitrogen-Rich Energetic Materials, First Edition. Edited by Michael Gozin and Leonid L. Fershtat.

1.2.1 Arylpentazoles (ArN_5)

For a long time, arylpentazoles (ArN_5), which are usually stored at low temperatures, were the only experimentally known substituted pentazoles. The first attempt to synthesize ArN_5 was carried out in 1903; however, it was only in the 1950s that the existence of ArN_5 was established through kinetic and gas-volumetric methods [8, 9]. The crystal of *p*-dimethylaminophenylpentazole (DMAP-N_5), which owns a room-temperature decomposition point, is the first and only direct evidence for the existence of substituted pentazoles [10].

The stabilities of para and ortho/para-substituted phenylpentazoles (PhN_5) were explored. It was confirmed computationally that ArN_5 is stabilized by the addition of an electron-donating group and destabilized by the addition of an electron-withdrawing group at the para position of the benzene ring. The stabilizing effects of electron-donating groups have been shown to arise through resonance interactions with the electron-deficient pentazole ring, while the decomposition of ArN_5 to N_2 and the corresponding azide was established to be a first-order reaction. The calculated dissociation energies of the N—N bonds in these substituted ArN_5 were determined to be 109–117 kJ mol^{-1}, which are higher than those of PhN_5, but are far lower than the activation energy (362–402 kJ mol^{-1}) for cleavage of the C—N bond that links the benzene and pentazole rings (Figure 1.1) [12].

Derivatives of PhN_5 substituted with alkali metals (M = Li, Na, and K) at the para-, meta-, or ortho-positions of the benzene ring were designed by Gong et al. The metal substituents improved the energy barrier for decomposition of the N_5 ring of PhN_5 by 19.3–65.0 kJ mol^{-1} (K > Na > Li) [12–14]. In particular, a new ionic N—M

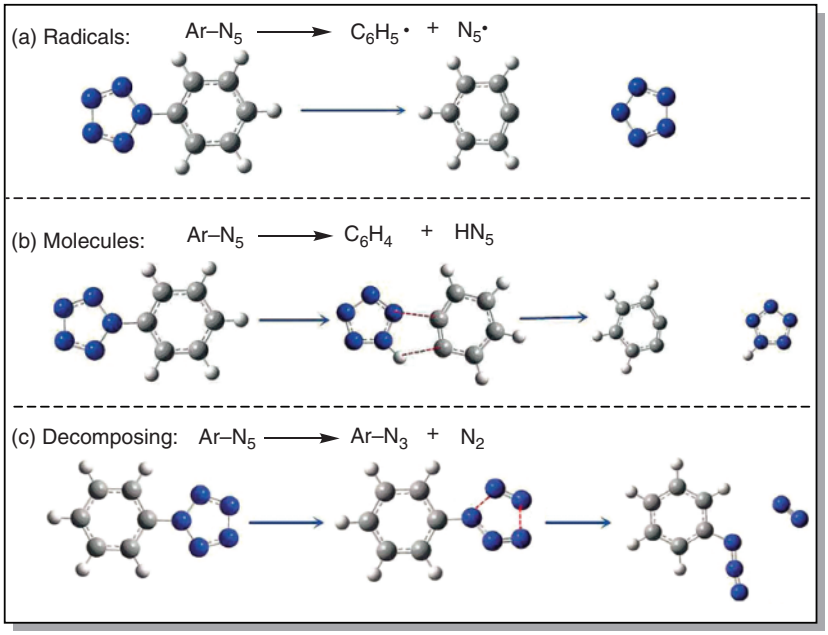

Figure 1.1 (a, b) Two possible pyrolysis paths of the C—N bond of ArN_5; (c) decomposition of the *cyclo*-N_5^- ring of ArN_5. Source: Bondarchuk [11]/with permission of Royal Society of Chemistry.

bond is observed between the metal and N_5 in the ortho-substituted PhN_5, which is not observed for the para- or meta-substituted derivatives. The strong intramolecular interactions in the ortho-substituted PhN_5 generate more negative charge on the pentazole ring, which strengthens dispersion interactions, resulting in higher pentazole-ring stability.

1.2.2 Heterocycle Pentazoles

It appears to be much more difficult to attach heterocyclic rings to pentazole, compared to aryl rings. Tetrazolylpentazole was the second type of pentazole derivative prepared, but it decomposes quickly at −50 °C and can only be confirmed by low-temperature ^{15}N-NMR spectroscopy. Calculations show that the tetrazole substituent has a similar conjugation effect to that of aryl, as is commonly observed for other azoles [15]. Since it is possible to remove an N–H proton from azolylpentazolate (AzN_5), anionic AzN_5 and its derivatives have been investigated. Anionic AzN_5 and its derivatives were found to exhibit lower decomposition energies and higher activation energies for decomposition than the corresponding neutral compounds, due to the higher electron densities of their pentazole rings.

The potential of pyridylpentazole and its pyridazylpentazole, triazinylpentazole, tetrazinylpentazole, and pentazinylpentazole derivatives to replace PhN_5 as a source of the pentazolate anion has been assessed [16]. Replacement of the aryl group of PhN_5 with a six-membered heterocycle weakens both the pentazole ring and the central C—N bond, as evidenced by the lower activation energies required to fragment the pentazole ring (8.4–30.8 kJ mol^{-1}) and the central C—N bond dissociation energies (11.3–21.0 kJ mol^{-1}). However, decreases in the C—N bond stability (2.1–7.8%) caused by the heterocyclic ring and its substituents are less obvious than those of the N_5 ring (12.7–23.7%); therefore, *cyclo*-N_5 substituted with six-membered heterocyclic rings are not likely to be better sources of *cyclo*-N_5^- than PhN_5.

1.2.3 Benzylpentazole (BzN_5)

BzN_5 and its derivatives have a methylene spacer between the pentazole and the benzene ring, which can be substituted by electron-donating (−NH_2, −NHMe, −NMe_2, and −OH) and electron-withdrawing (−NO_2, −CN, −CF_3, and −NF_2) groups, thereby endowing these molecules with a range of stabilities (Table 1.1). Substituents, especially electron-withdrawing groups, simultaneously lower the stabilities of the pentazole ring and the C—N bond in substituted BzN_5. Compared to ArN_5, computational studies show BzN_5 and its derivatives mostly possess lower activation energies for pentazole-ring decomposition (81.2–101.7 kJ mol^{-1}) and high C—N bond dissociation energy (385.6–452.8 kJ mol^{-1}), which is not suitable to replace ArN_5 as precursors of *cyclo*-N_5^- [13].

1.2.4 Other Substituted Pentazoles

Pentazoles have been substituted with other groups, such as –CH_3, –CN, and –NH_2, in either neutral (R–N_5) or cationic (R–N_5H^+) forms, and as *N*- and *N*,*N*′-oxide pentazole-based derivatives [17, 18] (Figure 1.2). Some of these compounds exhibit

Table 1.1 Difference between E_a of BzN_5 derivatives and PhN_5.

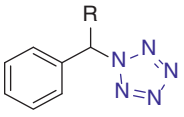

R = –H, R = –NH_2, R = –$NHCH_3$, R = –$N(CH_3)_2$, R = –OH, R = –NO_2, R = –CN, R = –CF_3, R = –NF_2

	E_a (kJ mol^{-1})	$\Delta E_a'$ (kJ mol^{-1})	$\frac{\Delta E_a'}{E_a}$ (PhN_5) (%)
BzN_5	101.7	13.0	14.7
–NH_2	97.2	8.5	9.6
–NHMe	96.2	7.5	8.5
–NMe_2	100.0	11.3	12.7
–OH	92.3	3.6	4.1
–NO_2	81.2	−7.5	−8.5
–CN	90.0	1.3	1.5
–CF_3	93.5	4.8	5.4
–NF_2	88.6	−0.1	−0.1

very attractive properties based on computational chemistry. For example, neutral methylpentazole is predicted to be as stable as the aromatic pentazole derivative; the pentazolium–nitrate pair provides high amounts of released energy, with a heat of reaction of ~130 kcal mol^{-1}; oxidized or nitrated pentazoles could serve as energetic oxidative materials. There is the strong possibility that these pentazole derivatives will lead to HEDMs; however, these molecules are not available with current experimental techniques; they are also potentially hazardous because of their high formation enthalpies and weak N—N bonds.

1.2.5 Polypentazoles Clusters

The pentazole ring is comparatively stable for a polynitrogen compound since it benefits from conjugation arising from electronic delocalization in the ring [19], and the separation of the σ- and π-electron systems [20]; therefore, the pentazole

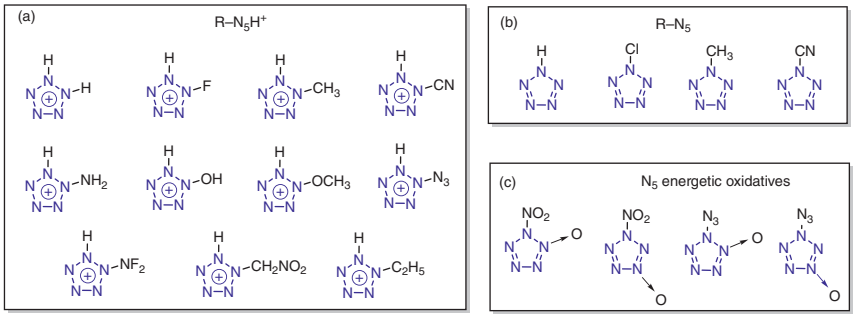

Figure 1.2 Other substituted pentazoles: (a) R–N_5H^+; (b) R–N_5 (R = H, Cl, CH_3, CN); (c) N_5 energetic oxidatives.

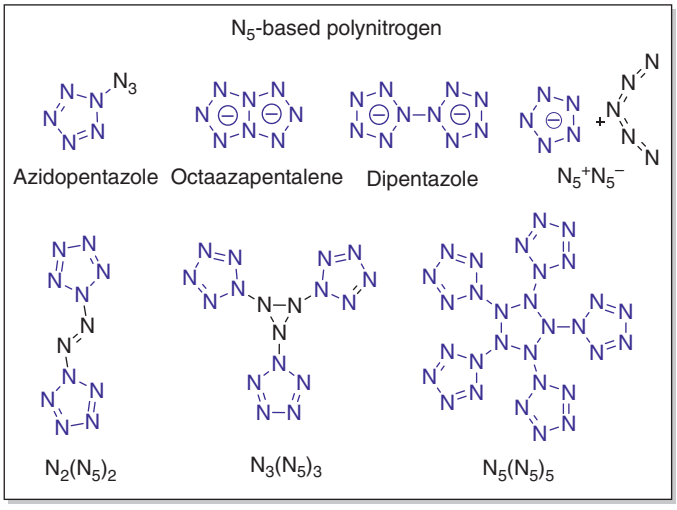

Figure 1.3 Polypentazoles clusters.

ring is a potentially useful building block for producing higher polynitrogen clusters (N_n). In the case of $5 < n \leq 10$, N_8 and N_{10} clusters involving pentazole ring represent minimum energy structures (Figure 1.3) [11, 21, 22]. Among them, $N_5^+N_5^-$, in particular, was previously highly hoped for, but subsequent calculations have shown that it is impossible to exist [5]. Born–Haber cycle-based stability estimates that $N_5^+N_5^-$ will decompose to vibrationally unstable species upon neutralization, by using adiabatic ionization potentials and electron affinities. Other pentazole-ring-containing polynitrogen (N_n) clusters ($n > 10$), which include N_{11}–N_{15}, and N_{18} multiple-ring structures ($N_3(N_5)_3$), N_{20} ($(N_5)_4$), N_{30} ($N_5(N_5)_5$), are all theoretically more stable as clusters than as open-chain structures. The N_{11}–N_{15} structures are composed of one or two pentazole rings connected by chains of three, four, or five nitrogen atoms. These clusters are 5–7 kcal mol^{-1} lower in energy than their corresponding open-chain structures, and their decomposition barriers are as low as 5–10 kcal mol^{-1} under most conditions. The structures containing multiple pentazole rings, namely N_{18}, N_{20}, and N_{30}, are 200–400 kcal mol^{-1} lower in energy than their corresponding cages, and their dissociation energies were determined to be 50–60 kcal mol^{-1}. The improved stabilities of the multiple pentazole-ring-containing structures compared to the single ring structures suggest that N_{60} should exist. N_{60} is analogous to C_{60} and is predicted to have a heat of formation of 6790 kJ mol^{-1} [2].

1.3 Strategies for the Preparation of *cyclo*-N_5^-

There are two routes for preparing pentazolate anion. One way is cleaving the C—N bond in ArN_5 to form *cyclo*-N_5^-, the other way is directly generating through *in situ* [3+2] cyclization between N_3^- and N_2. However, both approaches have great technical bottlenecks; the previous one needs to overcome the problem that the N—N bond is more unstable than the C—N bond and the pentazole ring is easy to destroy during

the cleaving process and the second way requires great energy to activate N≡N triple bond so that it can react with N_3^-. So far, many attempts have been reported, and we can classify them into three categories.

1.3.1 Using High-Energy Electrons to Cleave the C—N Bond in ArN_5

Strategies for the preparation of *cyclo*-N_5^- with high-energy electrons have been designed as follows: (i) ArN_5 bearing highly electron-donating substituents in the para-position of the benzene ring should be prepared as starting materials. In this manner, the aromaticity and stability of the *cyclo*-N_5^- ring can be increased by transferring maximum amounts of electron density to the *cyclo*-N_5^- ring, while simultaneously weakening the connective C—N bond. (ii) The C—N bond should be selectively cleaved by high-energy electrons while maintaining intact N—N bonds in the *cyclo*-N_5^- ring. High-energy electrons can be obtained from tandem mass spectrometry (MS–MS) using collision-induced dissociation (CID) at high collision voltages, laser irradiation, and strong UV–vis/Raman spectra.

In 2002, *cyclo*-N_5^- was first detected in mass-spectrometry experiments (Figure 1.4) [7] in which a ArN_5 was dissolved in strongly polar solvents and injected into the mass spectrometer with a syringe pump. The desired *cyclo*-N_5^--ion peak was observed by tandem mass spectrometry (MS–MS), using CID at high collision voltages, and at low collision voltages fragmentation to the azide was seen. This method was further modified by Östmark, who observed the *cyclo*-N_5^- signal directly from a solid sample of ArN_5 by laser irradiation in a vacuum [23].

The two results elucidated a possible reaction pathway for a single electron transfer mechanism (SET) and the radical anion acted as an important intermediate. Hence, researchers attempted to photochemically produce *cyclo*-N_5^- in either solid or liquid phases, using different types of lasers. With UV–vis and Raman spectra providing *in situ* analytical technologies, the important decomposition intermediates and overall quantum yields, as well as the end product distributions, were determined [24–27]. These researchers found that, although the photochemistry of ArN_5 is characterized

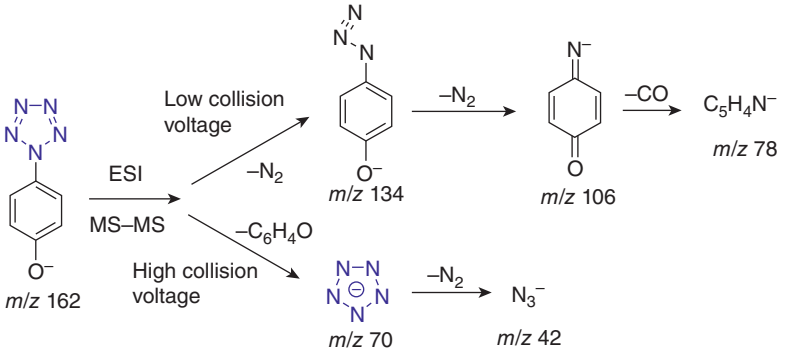

Figure 1.4 Experimental detection of the pentazolate anion. ESI–MS–MS fragmentation observed for the mass-selected ^{15}N singly labeled 4-pentazolylphenolate anion at low and high collision voltages.

by a range of reaction pathways when performed under a variety of conditions, the azide and azophenyl derivatives were the major products in all cases. It appears that the critical factor that drives the reaction is actually the formation of the radical through electron transfer, rather than the photoexcitation step itself.

1.3.2 Cleaving the C—N Bond of ArN_5 Using Redox Chemistry

The redox reaction is the most commonly used method for electron transfer and further leading to chemical cleavage in synthetic chemistry. Ceric ammonium nitrate (CAN) was the first used oxidant and SET reagent, while $Zn(NO_3)_2$ was added to stabilize and capture *cyclo*-N_5^-. ^{15}N-NMR spectroscopy revealed a novel signal at -10.0 ± 2.0 ppm. According to the calculated chemical shifts of $Zn(N_5)Cl$ and $ZnN_5(NO_3)$ (-16 and -17 ppm, respectively), and other possible ions present in the solution, $ZnN_5(NO_3)$ was concluded to have been generated. But repeated experiments attributed the signal at -10.0 ppm to the NO_3^- anion because it could also be observed in the absence of any other nitrogen-containing compound [28]. To confirm whether *cyclo*-N_5^- is generated, the ^{15}N-labeled ArN_5 is prepared and then tested. Although no signal for the N_5^- anion was detected, ^{15}N-labeled N_3^- ions were detected for all samples, confirming that they arose from the degradation of N_5^- in solution [29].

Later, N_5^- was accurately directly detected for the first time in 2016, by alkali metal treatment of ArN_5 at low temperature. Since they readily donate electrons, alkali metals are good reducing agents; consequently, they can convert phenylpentazole into the corresponding radical anion under mild conditions, after which thermal dissociation produces *cyclo*-N_5^-, as evidenced by an MS signal at $m/z = 70$. The assignment of this signal to N_5 is further supported by single and double labeling with ^{15}N, which led to signals at $m/z = 71$ and 72, respectively. A dissociation product with $m/z = 42$, which could be assigned to N_3^-, was observed through further MS analysis of the $m/z = 70$ signal (Figure 1.5) [30, 31].

Another successful example of oxidative cleavage was reported in 2017 [32, 33] in which the N_5^- anion was obtained through cleavage of ArN_5 in a ferrous bisglycinate $Fe(Gly)_2$/*m*-chloroperbenzoic acid (*m*-CPBA) system (Figure 1.6). $Fe(Gly)_2$ and *m*-CPBA form a peroxide intermediate, which functions both as the redox site and a source of electrons, a consequence of the co-existence of Fe and the peroxide group. In contrast to the previous heterogeneous Na/Na_2O system in acetonitrile, $Fe(Gly)_2$/*m*-CPBA is soluble in methanol, resulting in a homogeneous reaction as a consequence. This represents a significant improvement in conditions that realized the cleavage of the *cyclo*-N_5^- anion as well as the isolation of a pentazole as the NaN_5 as a solid product in 9% yield after careful post-treatment and purification. The *cyclo*-N_5^- produced in this manner exhibited acceptable stability under common conditions and decomposed at 116.8 °C, which is superior to that of N_5^+ (above 70 °C) but inferior to that of N_3^- (above 400 °C) [34]. Theoretical study suggested a new proton-transfer pathway for this reaction system involving the radical anion, but the pathway involving direct cleavage of the C—N bond in ArN_5 still dominates kinetically [35–37].

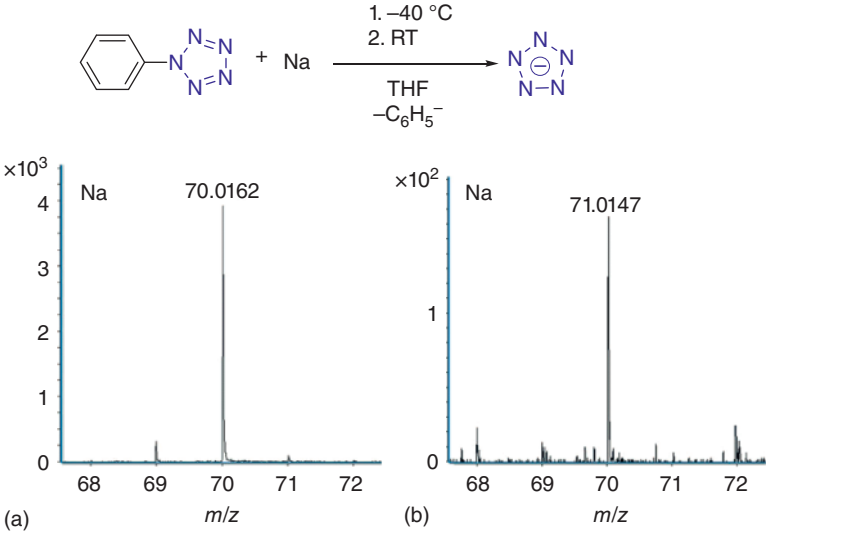

Figure 1.5 The HPLC/MS mass spectrum observed upon heating a solution of the PhN_5 radical anion in THF to room temperature for a short period of time (30–300 seconds); the spectrum was recorded 2.1 minutes after injection into the HPLC column: (a) using the all-^{14}N PhN_5, the spectrum is assigned to *cyclo*-$^{14}N_5^-$, (b) using $^{14}N_4{}^{15}N_1$-phenylpentazole, the spectrum is assigned to *cyclo*-$^{14}N_4{}^{15}N^-$. Source: Butler et al. [9]/with permission of John Wiley & Sons.

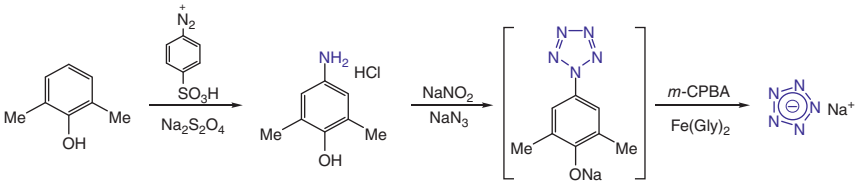

Figure 1.6 Preparation of *cyclo*-N_5^- through cleavage of ArN_5 in $Fe(Gly)_2$/*m*-CPBA system.

1.3.3 Possible [3+2] Reaction of N_3^- and N_2 at High Pressure

In addition to C—N bond cleavage of ArN_5 to generate *cyclo*-N_5^-, Oleynik et al. reported another possible strategy for the production of *cyclo*-N_5^-, in which azide salts and cryogenic liquid N_2 were laser heated in a diamond anvil cell at super high pressure at 60 GPa. The laser provided sufficiently high energy to overcome the [3+2]-cyclization barrier, while the high pressure prevented the decomposition of *cyclo*-N_5^- [38–42]. From then on, many research groups followed up the study of high-pressure preparation pentazole and its congeners [43–46]. The extreme conditions limited direct experimental characterization; consequently, DFT-calculated XRD patterns and Raman spectra provided evidence for the formation of *cyclo*-N_5^-. Unfortunately, *cyclo*-N_5^- salts were not observed when the pressure in the diamond anvil cell was released, which is inconsistent with the results from the organic-synthesis strategy under ambient conditions.

1.4 Complexes of Metal and *cyclo*-N_5^-

The theoretical study of metal and *cyclo*-N_5^- complexes has a long history. Their results indicate that metal ions can stabilize *cyclo*-N_5^- in different forms. The physicochemical properties of the assembled metal complexes were computationally studied. These studies show that *cyclo*-N_5^- metal complexes have high kinetic stability and high energy, which means that the complexes have great potential as HEDMs.

This part will introduce the synthesis of metal-pentazole compounds at low temperature and atmospheric pressure, and the structure and related physicochemical properties of series metal-pentazole compounds.

Since metals, especially transition metals, usually coordinate effectively to nitrogen, metal-pentazolate compounds were further experimentally investigated in order to access the newly synthesized *cyclo*-N_5^- anion. To date, 14 types of metal–N_5 complexes have been prepared (Figure 1.7). Here, we divide these complexes into salts (0D) and metal–inorganic frameworks (MIFs, 1D and 3D) and coordination polymers (CPs) according to their dimensions.

1.4.1 Metal Salts of *cyclo*-N_5^- (0D)

When appropriate metal salts are dissolved into ethanol solutions containing the sodium salt of *cyclo*-N_5^-(**1-1**), $[Mn(H_2O)_4(N_5)_2]\cdot 4H_2O$ (**1-2**), $[Fe(H_2O)_4(N_5)_2]\cdot 4H_2O$ (**1-3**), $[Co(H_2O)_4(N_5)_2]\cdot 4H_2O$ (**1-4**), $[Zn(H_2O)_4(N_5)_2]\cdot 4H_2O$ (**1-5**), or $[Mg(H_2O)_6(N_5)_2]\cdot 4H_2O$ (**1-6**) formed through metathesis reactions between NaN_5 and $MnCl_2$, $FeCl_2$, $Co(NO_3)_2$, $Zn(NO_3)_2$, or $MgCl_2$, respectively [32, 47]; the single-crystal structures of these compounds are shown in Figure 1.8.

Complexes **1-2** to **1-5** crystallize in the orthorhombic *Fmmm* space group, with almost identical unit-cell arrangements (*a*: 12.144–12.342 Å; *b*: 17.114–17.444 Å; *c*: 6.465–6.570 Å; α: 90°; β: 90°; γ: 90°; *z*: 4). The pentagonal *cyclo*-N_5^- rings bind to the metal atoms (Mn, Fe, Co, or Zn) through η^1-coordination and appeared to be perfectly coplanar. The N—N bonds in the *cyclo*-N_5^- rings of the various complexes are not of equal length; the average N—N bond distances in **1-2** to **1-5** are 1.320, 1.329, 1.314, and 1.328 Å, respectively. Each metal ion (Mn, Fe, Co, or Zn in sp^3d^2 hybridization) contributes six empty orbitals to accommodate the lone pairs of electrons from the *cyclo*-N_5^- ligands, which are coordinated in a quadrilateral bipyramidal environment in which the axial positions are formed by two nitrogen atoms from two *cyclo*-N_5^- rings, and the equatorial planes are formed by four oxygen atoms from four coordinated water molecules. The ball-and-stick packing diagrams of **1-2** to **1-5** reveal that the metal–N_5 fragments are all stacked face to face, with interlayer distances of 3.269, 3.285, 3.233, and 3.268 Å (equal to *c*/2), respectively.

The structure of complex **1-6** contains a magnesium atom that is hydrated by six H_2O molecules and cannot coordinate to *cyclo*-N_5^-; therefore, each N atom in each *cyclo*-N_5^- is hydrogen bonded to H_2O, with the surrounding H_2O molecules providing a hydrophilic and polar environment that helps to stabilize and protect the *cyclo*-N_5^- rings in the crystal.

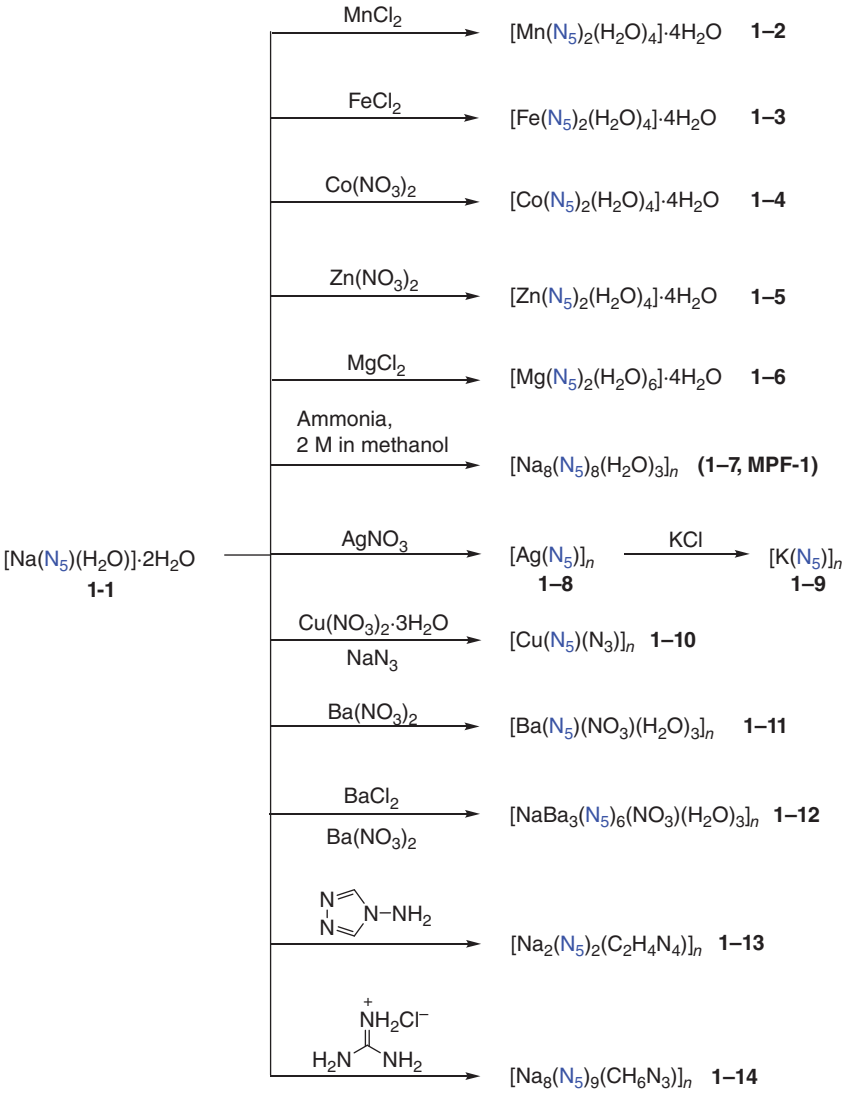

Figure 1.7 Synthesis route of *cyclo*-N_5^--metal complexes.

1.4.2 Metal–Inorganic Frameworks (MIFs) of *cyclo*-N_5^-

Adapting the procedure for C—N bond cleavage provided an air-stable, off-white NaN_5 hydrate, which was recrystallized to produce $[Na(H_2O)(N_5)]\cdot 2H_2O$ (**1-1**) [32]. Compound **1-1** exhibits a 1D MIF structure with orthorhombic C_{mcm} symmetry, with the pentagonal *cyclo*-N_5^- units adopting perfectly planar arrangements, as well as perfectly coplanar arrangements with adjacent sodium atoms. The *cyclo*-N_5^- anions and sodium ions in **1-1** are sequentially connected to form a saw-tooth-like 1D structure (Figure 1.9a–c).

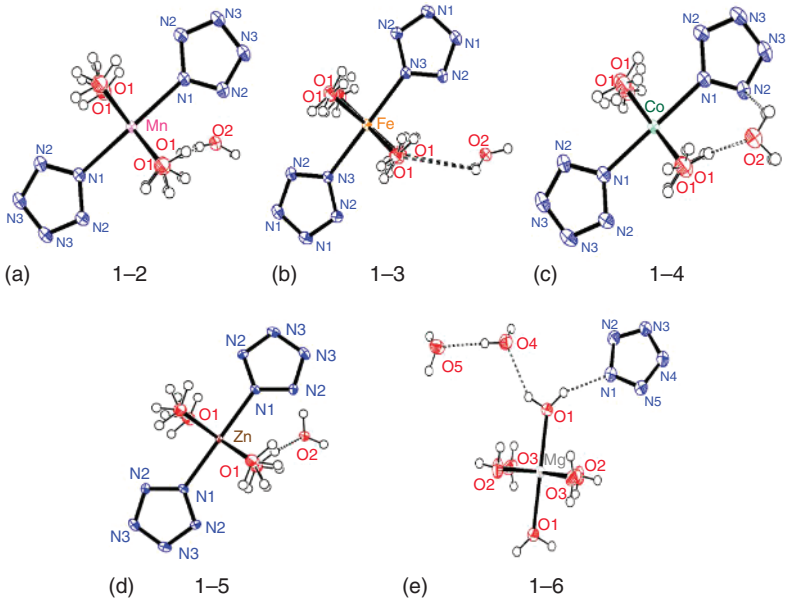

Figure 1.8 Single-crystal X-ray analyses of **1**-**5**, ellipsoids represent the 50% probability level. Source: Zhang et al. [12, 13]/with permission of Springer Nature. (a–c, e) (d) Xu et al. [47]/with permission of Royal Society of Chemistry.

A zeolite-like MIF with a fascinating 3D structure, namely $[Na_8(N_5)_8(H_2O)_3]_n$ (**1-7**), was successfully constructed from the 1D sodium-N_5^- framework by changing the pH conditions to weakly alkaline during recrystallization (Figure 1.9d–i) [48]. Twenty-four sodium ions, twelve *cyclo*-N_5^- rings, and twelve oxygen atoms form a drum-like nanocage, with one sodium ion in the center of the cage. Only one type of nanocage ($Na_{24}N_{60}O_{12}$) was observed in the single-crystal structure of **1-7**, while Zhang et al. synthesized a similar 3D framework (MPF-1) that exhibited two types of nanocages, namely $Na_{20}N_{60}$ and $Na_{24}N_{60}$ [49]. As shown in Figure 1.9j–l, the small $Na_{20}N_{60}$ cage is composed of 12 pentagons and 28 hexagons; the diameter of the $Na_{20}N_{60}$ nanocage is about 1.2 nm, while the larger $Na_{24}N_{60}$ nanocage contains 12 pentagons and 24 hexagons, and has a diameter of about 1.4 nm. The packing of the two types of nanocages results in a 3D framework with a zeolitic MEP topology (Figure 1.9m,n). When viewed in the *a*, *b*, and *c* directions, MPF-1 exhibits circular channels with 8.4-Å-sized pores. The total accessible volumes of **1-7** and **MPF-1** are 33.5% and 33.3% as calculated. As porous materials, **1-7** and **MPF-1** have calculated N_2-adsorption capacities of 2.59 and 2.5 mmol g^{-1} (1 atm and 273 K).

Aside from Na-based MIFs, *cyclo*-N_5^- and/or N_3^- and NO_3^- have been used as ligands, and self-assembly synthesis has been used to obtain additional 3D MIFs, such as $[Ag(N_5)]_n$ (**1-8**), KN_5 (**1-9**), $[Cu(N_5)(N_3)]_n$ (**1-10**), $[Ba(N_5)(NO_3)(H_2O)_3]_n$ (**1-11**), and $[NaBa_3(N_5)_6(NO_3)(H_2O)_3]_n$ (**1-12**) (Figure 1.10) [50, 51]. Each *cyclo*-N_5^- in **1-11** and **1-12** adopts a tridentate chelating mode to bridge three Ba cations, while *cyclo*-N_5^- adopts a quadridentate chelating mode to bridge four metal cations in **1-8**

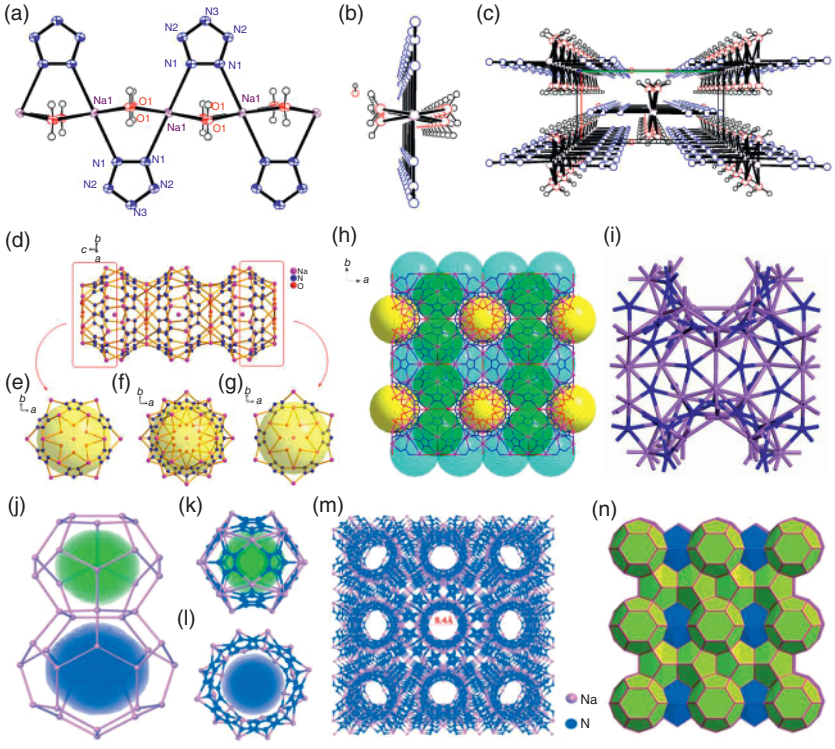

Figure 1.9 The structures of 1D MIF **1-1** (a–c), 3D porous MIFs **1-7** (d–i) and **MPF-1** (j–n). (a, b) Extended molecular view of **1-1** normal to (100) and (001), respectively; (c) Ball-and-stick packing diagrams of **1-1** viewed normal to (001) with hydrogen bonds; (d) Selected three $Na_{24}N_{60}O_{12}$ nanocages in **1-7** viewed along the *a* axis; (e) Half of a cage viewed along the *c** axis; (f) Selected three nanocages viewed along the *c* axis; (g) Half of a cage viewed along the *c* axis; (h) The 3D framework of **1-7**; (i) A schematic representation of the topology for **1-7**, in which the N_5 ligands are represented by blue spheres and the Na ions are represented by purple spheres; (j) The connected mode between $Na_{20}N_{60}$ and $Na_{24}N_{60}$ nanocages in **MPF-1**; (k) The structure of $Na_{20}N_{60}$ nanocage; (l) The structure of $Na_{24}N_{60}$ nanocage; (m) The 3D open framework of **MPF-1**; (n) the zeolitic MEP topology of **MPF-1**. Source: (a–c) Zhang et al. [12]/with permission of Springer Nature; (d–i) Zhang et al. [14]/with permission of Royal Society of Chemistry; (j–n) Zhang et al. [16]/with permission of John Wiley & Sons.

and **1-10**. The most interesting one is **1-9**, in which five N atoms in one *cyclo*-N_5^- coordinate with seven K ions.

1.4.3 Coordination Polymers

The guanidinium cation, $CN_3H_6^+$ (Gu^+), and 3-amino-1,2,4-triazole $C_2H_4N_4$ (ATz) were used instead of Na^+ to prepare nonmetallic salts, but they eventually formed CPs, namely $(NaN_5)_5[(CH_6N_3)N_5](N_5)_3^-$ (**1-13**) and $(NaN_5)_2(C_2H_4N_4)$ (**1-14**) (Figure 1.11). The crystal structures reveal the coexistence of the chelating *cyclo*-N_5^- and the organic component in the solid state. Na^+ and N_5^- are

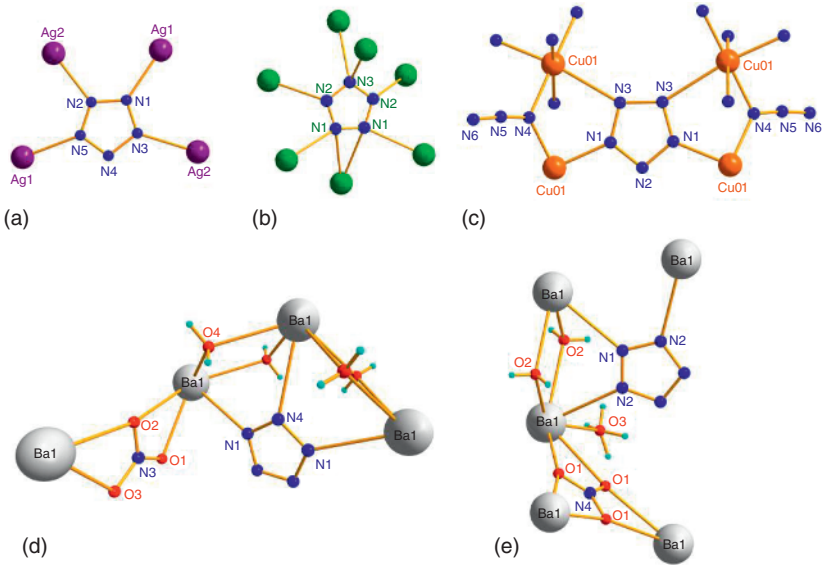

Figure 1.10 Coordination bond of *cyclo*-N_5^- captured from single-crystal X-ray analyses of **1-8** (a), **1-9** (b), **1-10** (c), **1-11** (d), and **1-12** (e). Source: Rahm and Brinck [17]/with permission of John Wiley & Sons.

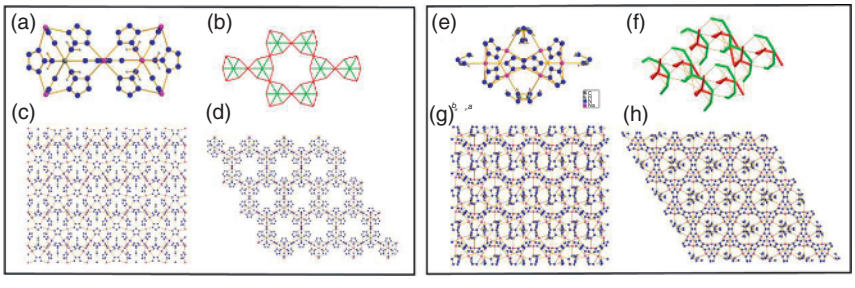

Figure 1.11 Single-crystal X-ray analyses of **1-13** (a–d) and **1-14** (e–h). (a) The coordination mode of Na^+, (b) A topological net of simplified unit cell, (c, d) Unit cell stacking diagram view along *b* and *c* axes (4*4*4) of **1-13**. (e) The coordination mode of Na^+, (f) A topological net of simplified unit cell, (g, h) Unit cell stacking diagram view along *b* and *c* axes (4*4*4) of **1-14**. Source: Zhang et al. [49]/with permission of Springer Nature.

coordinated to form a cage structure that traps the guanidinium cation $[C(NH_2)_3]^+$ in the $(NaN_5)_5[(CH_6N_3)N_5](N_5)_3^-$ CP. A mixed-ligand system is observed in the $(NaN_5)_2(C_2H_4N_4)$ CP; N_5^- and ATz are separately coordinated to Na^+ to form two independent but interwoven nets. Moreover, no crystallized H_2O is formed in these products, which are anhydrous compounds of *cyclo*-N_5^- salts with high heats of formation (>800 kJ mol^{-1}). The nitrogen contents and heats of formation of the two CPs are much higher than those of traditional energetic materials (TNT, RDX, and HMX). However, their detonation properties are not particularly good

when compared to those of TNT, RDX, HMX, and CL-20. The poor detonation performance of the two CPs is attributed to their low densities, a consequence of their porous structures. From another perspective, these porous structures could encapsulate other smaller energetic materials in order to improve energetic performance [52].

1.4.4 Structural Characterization

1.4.4.1 MS and NMR Characterization

The *cyclo*-N_5^- can give a signal of $m/z = 70$ in mass spectrometry and no fragments are observed, indicating that the structure has good stability. A concentrated reaction solution containing ^{15}N labeled *cyclo*-N_5^- rings marked using $Na^{15}NO_2$ was dissolved in deuterated methanol (CD_3OD-d_4) for liquid NMR analysis (Figure 1.12). The results showed that the N-NMR peak of *cyclo*-N_5 appeared at the chemical shift of −3.0 ppm. The chemical shift of the peak coincides with that of the theoretically calculated results in the literature (−6.5 to 0 ppm) [53–55]. Residual nitrate was detected at −12.4 ppm, which also agreed with previous results at -10 ± 2 ppm [56, 57].

1.4.4.2 Topology Analysis

The topology of *cyclo*-N_5^- in eight complexes (**1-7** to **1-14**) that own three-dimensional structures was analyzed. Their topology types and legends are shown in Table 1.2 and Figure 1.13. From the result, it can be found that *cyclo*-N_5^- constructs new topological types except complexes **1-8**. For complexes **1-7**, **1-13**, and **1-14**, they have the same metal and all have *cyclo*-N_5^- as the main ligand, but their topological types vary greatly.

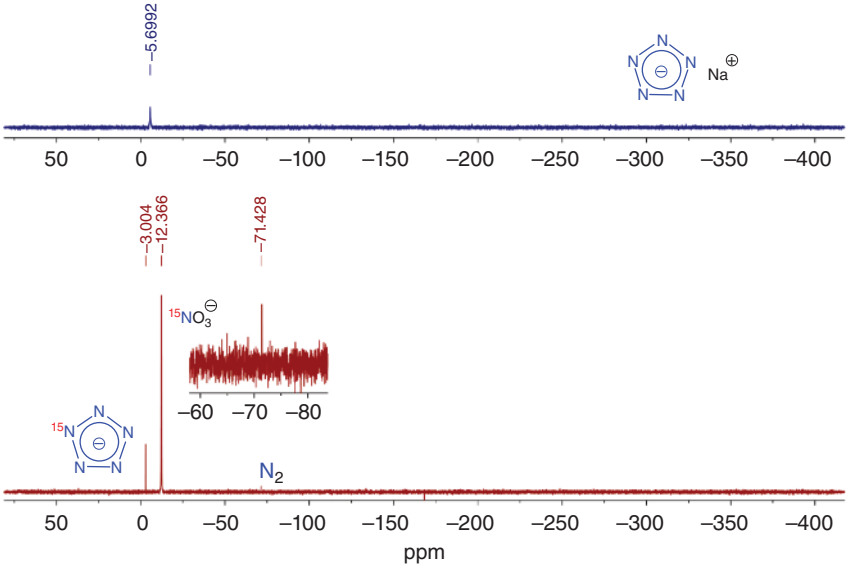

Figure 1.12 NMR spectra of the reaction solution of complex **1-1** and ^{15}N labeled NaN_5.

Table 1.2 Topology types of complexes **1-7** to **1-14**.

Complex	Topological type
1-7	$\{3.4^4.5^2.6^3\}_{12}\{3^2.4^4.5^2.6^2\}_{12}\{3^4.4^8.5^6.6^3\}_{12}\{3^8.4^8.5^8.6^4\}_3\{4^{12}.6^3\}_8$
1-8	PtS, $\{4^2.8^4\}$
1-9	$\{4^{15}.6^6\}\{4^{17}.6^4\}$
1-10	$\{3^2.6^2.7^2\}\{3^4.4^2.6^4.7^5\}$
1-11	$\{3^2.4\}\{3^4.4^3.5^2.6^{10}.7^2\}$
1-12	$\{3^2.4\}_3\{3^4.4^3.5^2.6.8^4.9\}_3\{8^3\}$
1-13	$\{3.4^4.5^2.6^3\}\{3^2.4^8.5^3.6^2\}$
1-14	$\{4^{12}.6^3\}_2\{4^2.6\}_6\{4^3.6^2.8\}_3\{4^6.8^4.10^5\}_3$

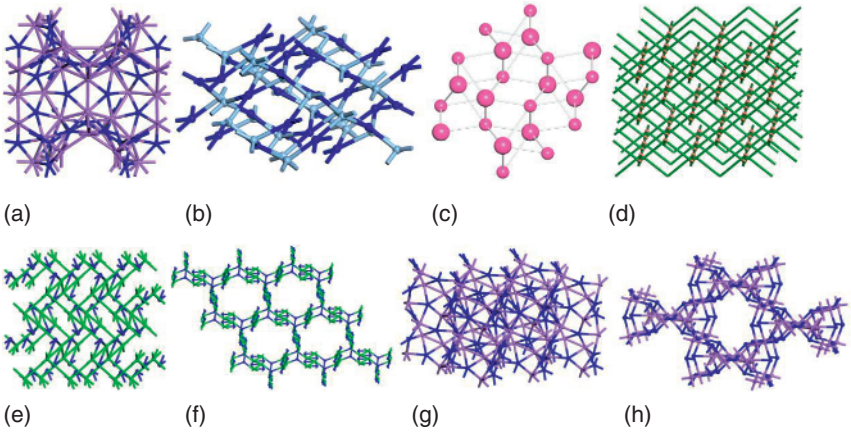

Figure 1.13 Topology types of complexes **1-7** to **1-14**.

1.4.4.3 Raman and IR Analysis

The *cyclo*-N_5^- was predicted to have a D_{5h} symmetry (A1′ + E1′ + 2E2′ + E2″), but indeed showed C_{2v} symmetry (A1 + (B2) + 2(A1 + B2) + (A2 + B1)). It is because that the geometry of *cyclo*-N_5^- in most complexes was affected by coordination mode and the N—N bond length changed. Among them, (A2 + B1) mode derived from E2″ has neither infrared nor Raman activity; (A1 + B2) mode derived from E1′ is infrared activity; the A1 and 2(A1 + B2) mode derived from A1′ and 2E2′ are Raman active (Figure 1.14). So, in theory, the *cyclo*-N_5^- ring with C_{2v} symmetry should have two infrared absorption peaks and five Raman peaks.

The infrared spectra of the 14 kinds of metal complexes measured experimentally are shown in Figure 1.15. The non-three-dimensional complexes (**1-1** to **1-6**) have two absorption peaks: 1244–1258 cm^{-1} (B2) and 1219–1238 cm^{-1} (A1). But the two absorption peaks of *cyclo*-N_5^- in three-dimensional complex (**1-7** to **1-14**) are not clearly split, presented as only one absorption peak, whose wave number was at 1217–1248 cm^{-1}.

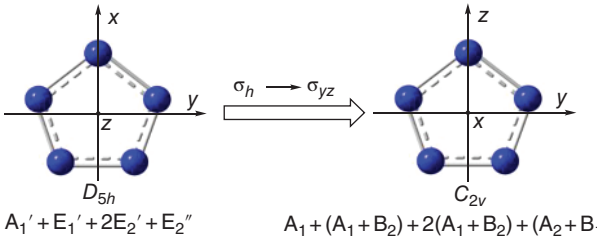

Figure 1.14 Transformation of D_{5h} to C_{2v} symmetry.

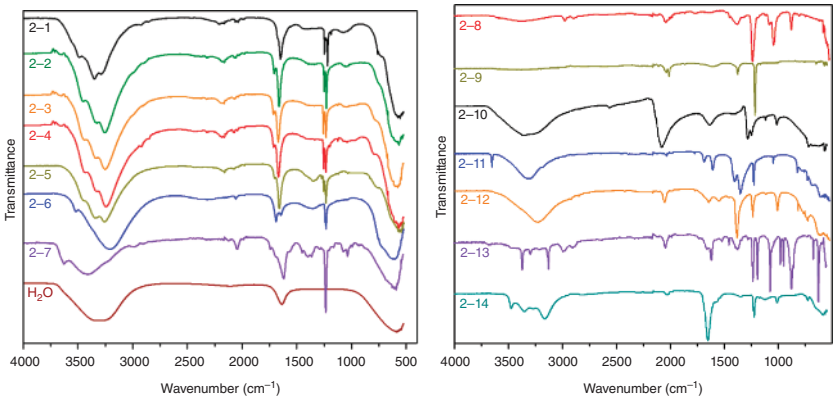

Figure 1.15 Infrared spectra of complexes **1-1** to **1-14**.

The Raman spectra of *cyclo*-N_5^- in these three-dimensional complexes (**1-7** to **1-14**) also could not clearly be defined. Since the three-dimensional complexes are microscopic porous structures, there will be solvents, N_3^-, NO_3^- in the cell gaps and pores, and thus the Raman spectrum is complex. The spectra of non-three-dimensional complexes (**1-1** to **1-6**) can be defined and shown in Figure 1.16 for Raman vibrations analysis. Theoretically, five Raman peaks of *cyclo*-N_5^- were corresponding to A1 and 2(A1 + B2) mode. The experimental results show that all six complexes have a strong peak in the range of 1188–1199 cm^{-1}, which was attributed to the A1 mode, 2(A1 + B2) modes should show four peaks, but three of them with low intensity are observed in Raman spectra, at a range of 1234–1239, 1120–1124, and 1005–1037 cm^{-1}.

1.4.4.4 Stability Analysis

Thermal stability is one of the most important properties of energetic materials. The most common methods to measure thermal stability are differential scanning calorimetry (DSC) and thermogravimetric (TG) analysis. Most of the *cyclo*-N_5^- complexes contain water in their crystals, and these water-containing samples have obvious dehydration and endothermic peaks before decomposition. The complexes **1-1** to **1-5** and **1-12** have only one obvious endothermic process before 150 °C, while for compounds **1-6** and **1-11**, three and two endothermic peaks were observed before

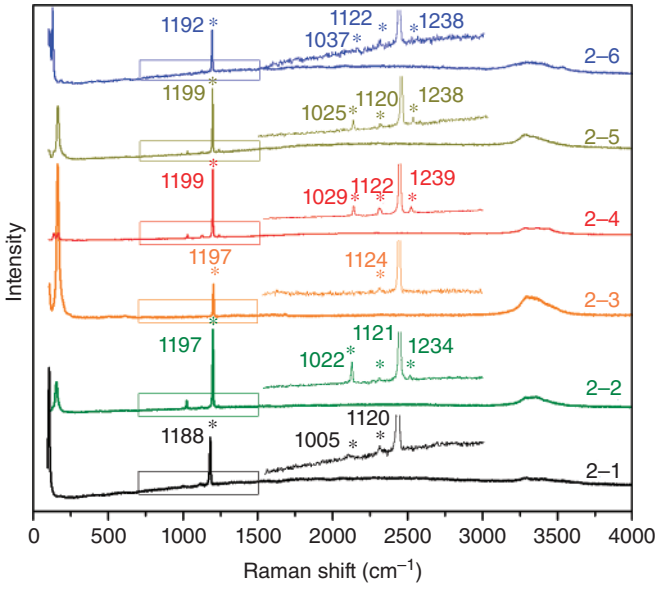

Figure 1.16 Raman spectra of non-three-dimensional complexes of *cyclo*-N_5^- .

the first exothermic peak (Figure 1.17). Except for **1-4** and **1-9**, all samples showed at least two exothermic stages. The first exothermic peak is similar and at a range of 90–130 °C, but the position of the second exothermic peak varies greatly. Among them, the first exothermic peak of the **1-11** and **1-12** complexes is continued to the previous endothermic peak, which means that it is not a simple decomposition process. For all the 14 complexes, the best thermal stability is complex **1-7** with a decomposition temperature up to 129.0 °C and the following two complexes are **1-13** and **1-14**. All these three compounds show three-dimensional structures and have sodium ion as the metal center and *cyclo*-N_5^- as the main ligand. Their thermal behaviors are also very similar; the first decomposition process of **1-7** has the highest heat release (373 J g^{-1}), followed by **2-13**(304 J g^{-1}) and **2-14**(280 J g^{-1}).

Based on a summary of the above studies on the thermal decomposition of *cyclo*-N_5^- complexes, it can be concluded that the thermal decomposition of the *cyclo*-N_5^- ring can be divided into two stages. The first stage is the breaking of two N—N bonds in the *cyclo*-N_5^- ring to decompose into stable N_2 and relatively stable azide ions; the second stage is the further decomposition of azide ions. Therefore, two obvious exothermic peaks can be observed in the DSC diagram of most complexes. In addition, there are two exceptions – complexes **1-4** and **1-9**. The first peak of complex **1-4** includes the exothermic process of water loss and the endothermic process of *cyclo*-N_5^- ring breaking. As thermal effects of water loss are greater than those of *cyclo*-N_5^- ring breaking, the comprehensive performance shows an endothermic peak. For complex **1-9**, after the first step decomposition of *cyclo*-N_5^- around 110–150 °C, the generated KN_3 shows good stability and undergoes only a melting process, which corresponds to an endothermic peak at

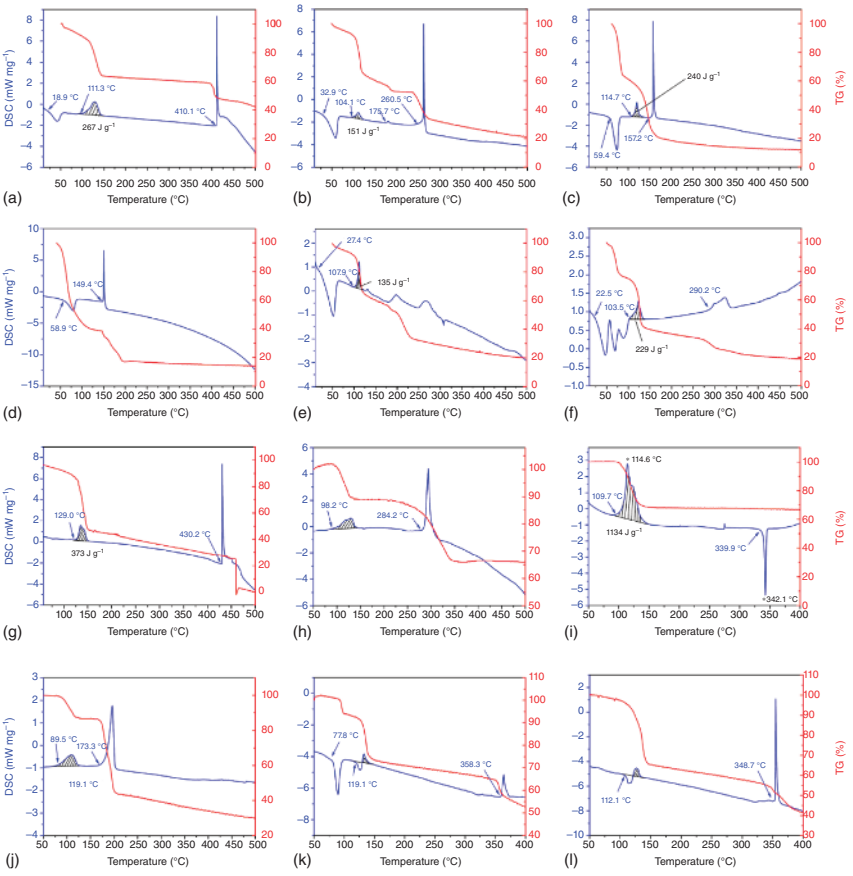

Figure 1.17 DSC and TG of complexes **2-1** to **2-12** (a–l).

342 °C without weight loss in TG. Meanwhile, no other exothermic peak is found even up to 400 °C.

The first decomposition process of these complexes, corresponding to *cyclo*-N_5^- decomposition, is undoubtedly the key step that has been the focus of attention. Further thermal kinetics tests were performed on **1-1**, **1-2**, **1-3**, and **1-6** (Figure 1.18). Based on DSC curves at different heating rates, the thermal decomposition activation energies *cyclo*-N_5^- in **1-1**, **1-2**, **1-3**, and **1-6** were obtained by the Kissinger method as 98.4, 106.6, 108.4, and 118.2 kJ mol^{-1} (Figure 1.19). The average thermal decomposition activation energy of *cyclo*-N_5^- complexes is about 108 kJ mol^{-1}, lower than that of nitroglycerin (209 kJ mol^{-1}), PETN (197 kJ mol^{-1}), picric acid (240 kJ mol^{-1}), etc.

1.4.4.5 Bonding Study

To investigate the relationship between the stability and structure of *cyclo*-N_5^- complex, the bonding condition in its crystal structure was analyzed. The formed coordination bonds and hydrogen bonds of each N atom in *cyclo*-N_5^- ring are shown in Figures 1.20 and 1.21. According to the bonding situation, all the complexes can be

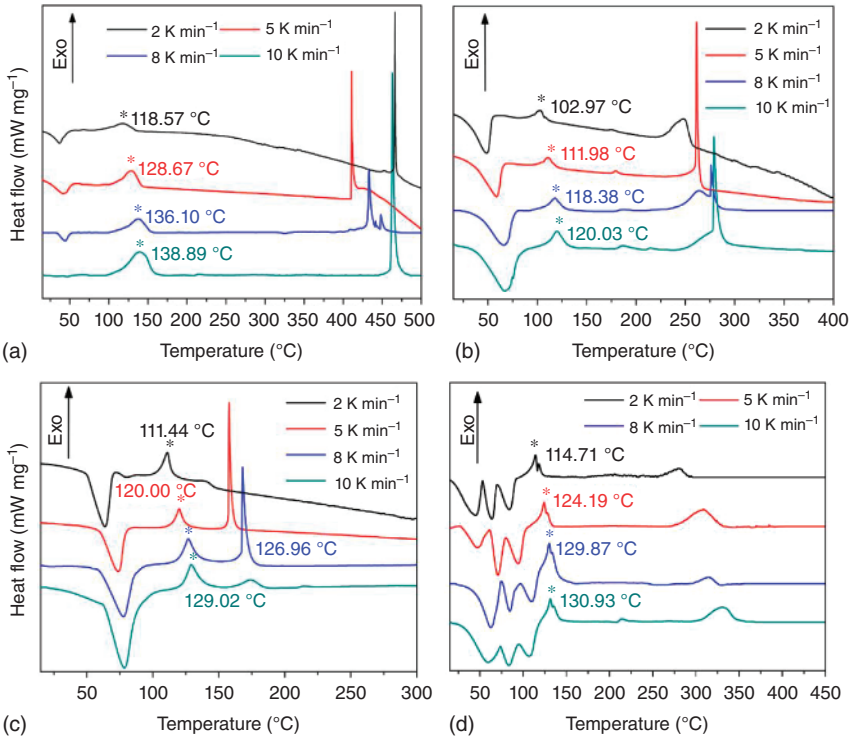

Figure 1.18 DSC curves of complexes **1-1**, **1-2**, **1-3**, and **1-6** (a–d) at different heating rates.

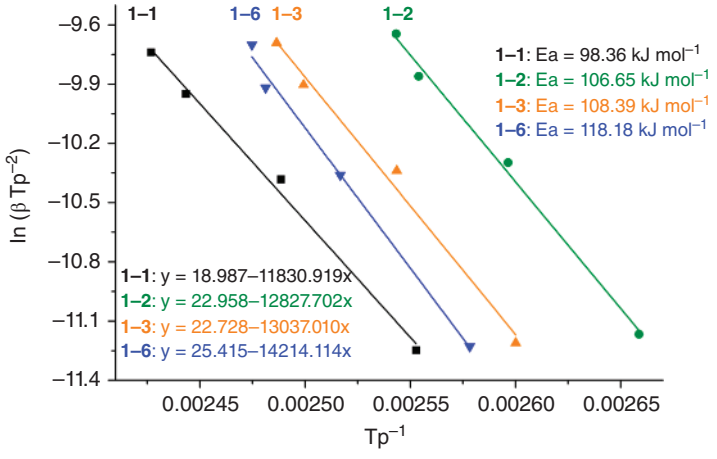

Figure 1.19 Apparent activation energy of first exothermic peak of complexes **1-1**, **1-2**, **1-3**, and **1-6** calculated with Kissinger method.

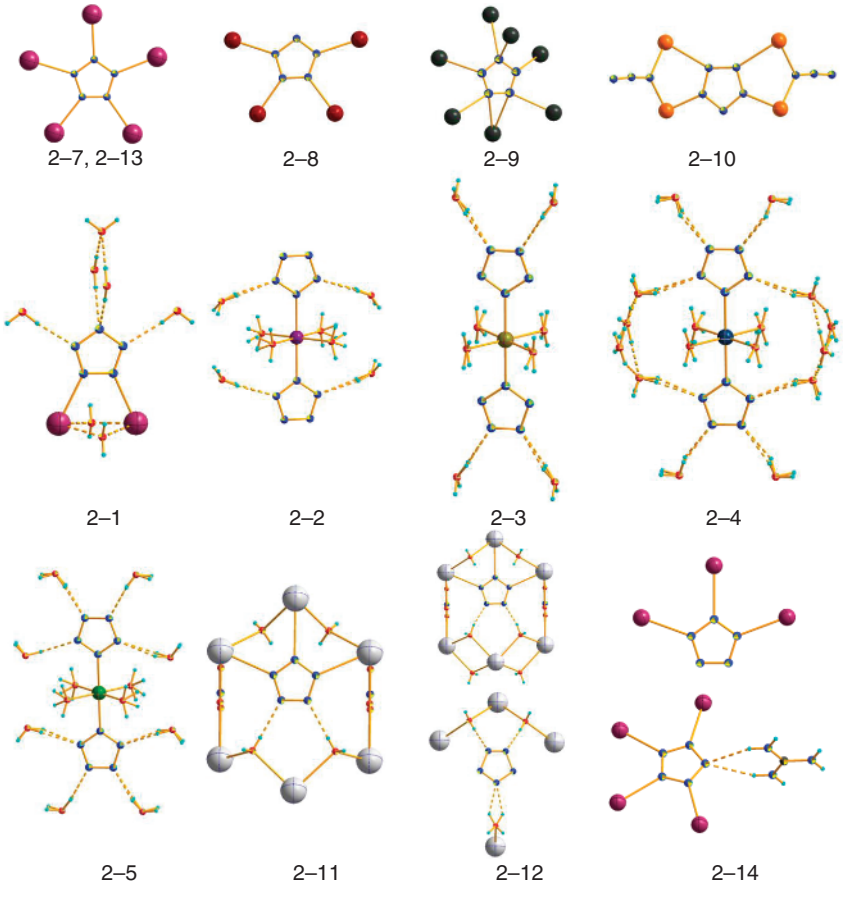

Figure 1.20 Bonding form of *cyclo*-N_5^- in complexes **1-1** to **1-5**, **1-7** to **1-14**.

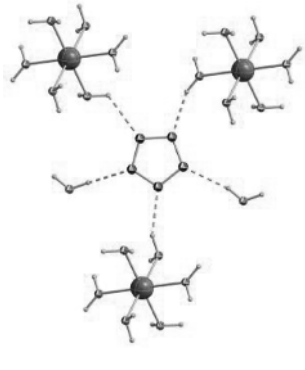

Figure 1.21 Bonding form of *cyclo*-N_5^- in complexes **1-6**.

divided into three classes: (i) coordination bond only, (ii) mixed coordination and hydrogen bond, and (iii) hydrogen bond only.

(1) **Coordination bond.** For complexes **1-7** to **1-10** and **1-13**, there is only a coordination bond found around *cyclo*-N_5^- in their crystals. In complexes **1-7** and **1-13**, the five N atoms in *cyclo*-N_5^- form η^1–σ coordination bonds with five metal ions. In complexes **1-8** and **1-10**, the four N atoms in *cyclo*-N_5^- participate in bonding in η^1–σ form with four metal ions. In complex **1-9**, the five N atoms in *cyclo*-N_5^- form six η^1–σ and two η^2–σ coordination bonds with seven metal ions.

(2) **Mixed coordination and hydrogen bonds.** For hydrous complexes **1-1** to **1-5**, **1-11**, and **1-12**, except for η^1–σ coordination bonds, there are also weak hydrogen bonds interaction between coordination or crystalline water and N atom in *cyclo*-N_5^-. Each *cyclo*-N_5^- prefers to form 1–3 coordination bonds with metal ions and then fills up with 2–4 O—H…N hydrogen bonds with water molecules. Whenever the two kinds of bond combine, *cyclo*-N_5^- ring always maintains the N_5 ring centered axisymmetric structure. Complex **1-12** has two types of *cyclo*-N_5^-, one type has the same bonding condition as that in **1-11**, and the other only has O—H…N hydrogen bonding. Complex **1-14** also contains two types of *cyclo*-N_5^-, one has three N atoms involved in coordination, the other has four N atoms involved in coordination, and one N atom forms N—H…N hydrogen bonds with guanidine cations.

(3) **Hydrogen bonding only.** In complex **1-6**, each N atom in *cyclo*-N_5^- forms a O—H…N hydrogen bonds with water molecules and is *cyclo*-N_5^- immobilized in a hydrogen bond network, which is similar to the second type in **1-12**. For many aqueous complexes, the loss of water will cause the decomposition of *cyclo*-N_5^-, indicating that water plays a very important role in the stability of *cyclo*-N_5^-.

To analyze the stabilizing effect of coordination water on the complex, the molecular orbitals of **1-5** with and without coordination water are calculated by quantum chemistry. It can be found that coordination water was involved in the coordination process by forming new orbitals with metals and pentazoles (Figure 1.22). Complexes **1-2**, **1-3**, and **1-4** were studied by the same method, and the same conclusion can be obtained.

1.4.4.6 Detonation Properties

Solid-state heat of formations (HOFs) is the most important parameter to calculate the detonation properties of energetic salts. For M_pX_q-type energetic complexes, the solid-state HOFs can be calculated according to the Born–Haber energy cycle [58]. For coordination polymers, the solid-state HOFs calculated based on experimental combustion enthalpy are more suitable. According to the combustion enthalpy and experimental HOFs of combustion products, the standard HOFs of coordination polymers can be calculated [59–61].

The detonation parameters such as detonation velocity can be calculated by EXPLO5 software [62] or K–J equation according to the calculated HOFs and the density under 298.15 K. Take **1-8** and **1-9** as examples: the calculated explosive

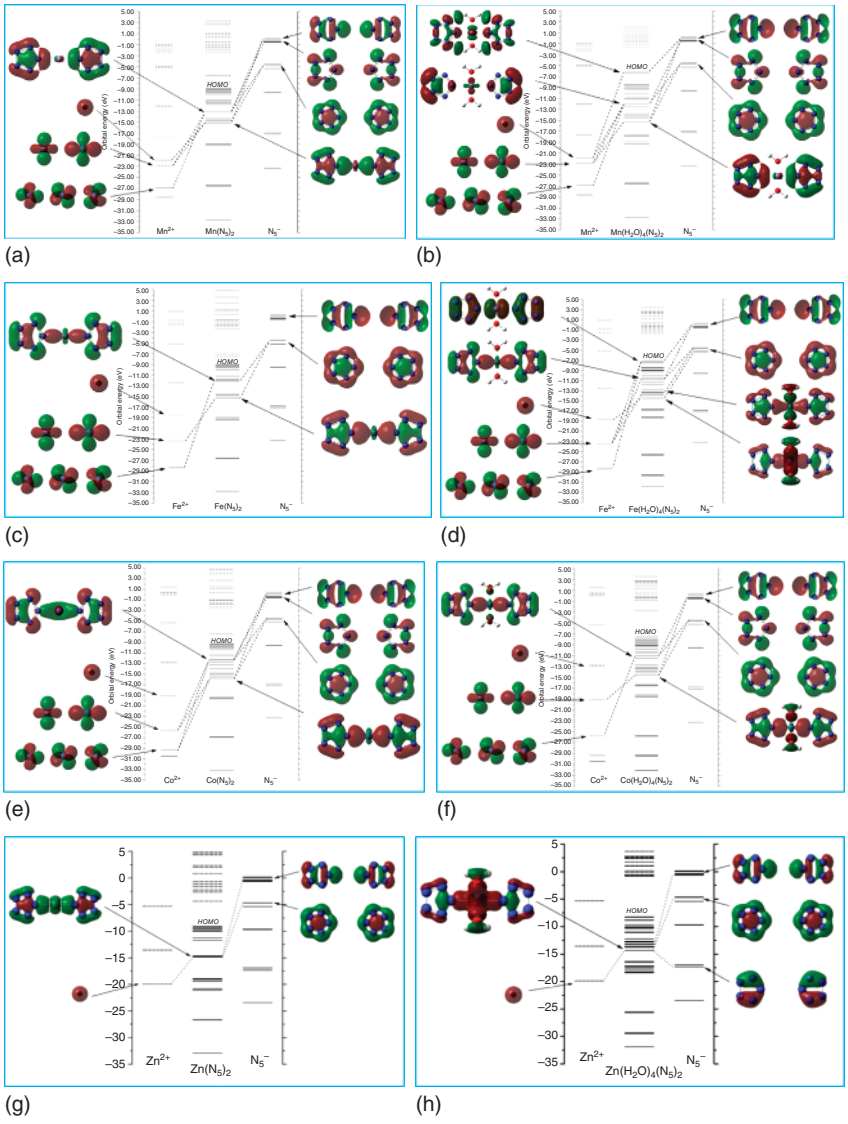

Figure 1.22 The molecular orbitals of **2-2** to **2-5** with and without coordination water.

heat (Q) of **1-8** is 1.110 kcal g^{-1}, the detonation velocity (D) is 7782 m s^{-1}, and the detonation pressure (P) is 34.67 GPa; the Q of **1-9** is 0.75 kcal g^{-1}, D is 6636 m s^{-1}, and P is 19.81 GPa. The detonation performance of **1-8** calculated by EXPLO5 is higher than that calculated by the K–J equation ($D = 6977$ m s^{-1}, $P = 20.9$ GPa). Their performances are superior to the reported two-dimensional frame material CHHP and ZnHHP [63], Ag complexes $[(atrz)_{1.5}(NO_3)]_n$ [64], and $[Ag(atz)]_n$ [59] as well as the detonation properties of explosive TNT [65] (Table 1.3).

Table 1.3 Physical and chemical properties of prepared pentazole derivatives.

Compound	Molecule formation	d[a] ($g\ cm^{-3}$)	T_d[b] (°C)	N[c] (%)	OB[d] (%)	ΔH_f[e] ($kJ\ mol^{-1}$)/ ($kJ\ g^{-1}$)	Q[f] ($kcal\ g^{-1}$)	D[g] (m s-1)	P[h] (GPa)	IS[i] (J)	FS[j] (N)	Reference
1-1	$[Na(H_2O)(N_5)]\cdot 2H_2O$	1.44/ 1.471(170 K)	111	47.62	−5.4							[32]
1-2	$[Mn(H_2O)_4(N_5)_2]\cdot 4H_2O$	1.59/ 1.608(205 K)	104	41.30	−4.7							[32]
1-3	$[Fe(H_2O)_4(N_5)_2]\cdot 4H_2O$	1.58/ 1.599(205 K)	115	41.19	−4.7							[32]
1-4	$[Co(H_2O)_4(N_5)_2]\cdot 4H_2O$	1.66/ 1.696(170 K)	59	40.82	−4.7							[32]
1-5	$[Zn(H_2O)_4(N_5)_2]\cdot 4H_2O$	1.65/ 1.669(205 K)	108	40.07	−4.6							[47]
1-6	$[Mg(H_2O)_6(N_5)_2]\cdot 4H_2O$	1.42/ 1.437(205 K)	104	40.66	−4.6							[32]
1-7	$[Na_8(N_5)_8(H_2O)_3]_n$	1.26/ 1.301(100 K)	129	70.19	−8.0	879/ 1.10	0.664	5.011	8.8			[48]
1-8	$[Ag(N_5)]_n$	2.96/ 3.015(173 K)	98	39.37	−4.5	827/ 4.65	4.644	7782	34.7	0.5	1	[42]
1-9	KN_5	1.96/ 2.002(150 K)	110	64.17	−7.3	136.8/ 1.25		6977	20.9	5	40	[51]
1-10	$[Cu(N_5)(N_3)]_n$	2.57/ 2.623(173 K)	90	63.81	−9.1							[50]
1-11	$[Ba(N_5)(NO_3)(H_2O)_3]_n$	2.52/ 2.592(100 K)	130[k]	25.91	+9.9	−914/ −2.83						[50]

(Continued)

Table 1.3 (Continued)

Compound	Molecule formation	$d^{a)}$ (g cm^{-3})	$T_d{}^{b)}$ (°C)	$N^{c)}$ (%)	OB$^{d)}$ (%)	$\Delta H_f{}^{e)}$ (kJ mol^{-1})/ (kJ g^{-1})	$Q^{f)}$ (kcal g^{-1})	$D^{g)}$ (m s-1)	$P^{h)}$ (GPa)	IS$^{i)}$ (J)	FS$^{j)}$ (N)	Reference
1-12	$[NaBa_3(N_5)_6(NO_3)(H_2O)_3]_n$	2.27/ 2.338(100 K)	121$^{k)}$	44.71	−0.8	−6249/ −6.43						[50]
1-13	$[(NaN_5)_5(CH_6N_3)N_5](N_5)_3^-$	1.19/ 1.214(170 K)	118	83.48	−14.9	1015/ 1.26	0.329	4407	6.5			[52]
1-14	$(NaN_5)_2(C_2H_4N_4)$	1.70/ 1.728(173 K)	127	72.59	−41.5	902/ 6.68	1.650	7863	26.4			[52]
MPF-1	—	1.23/ 1.270(100 K)	129	72.15	−2.7							[49]
	FOX-12	1.75	201	46.89	−3.8	−355/ −1.70		8323	26.6	30	350	
	RDX	1.80	205	37.84	0.0	80/ 0.36	1.386	8748	34.9	7	120	
	TNT	1.65	244	18.50	−24.7	−59/ −0.26	0.897	7178	20.5	15	>353	

a) Recalculated from low-temperature X-ray densities $\{d_{298K} = d_T/[1 + 1.5 \times 10^{-4}(298 - T)]\}$. Values after slashes were crystal densities.
b) Onset decomposition temperature (5 °C min^{-1}).
c) Nitrogen content.
d) Oxygen balance. For carbon-containing compound, $OB = 1600(c - a - b/2)/M_W$, M_W = molecular weight.
e) Calculated heat of formation in solid state.
f) Calculated heat of detonation.
g) Calculated detonation velocity.
h) Calculated detonation pressure.
i) Impact sensitivity.
j) Friction sensitivity.
k) The exothermic peak is connected to the previous endothermic peak.

1.5 *cyclo*-N_5^--Based Nonmetallic Ionic Salts

1.5.1 Synthesis

The nitrogen-rich pentazolate salts, *N*-carbamoylguanidinium, and oxalohydrazinium, 4,4′,5,5′-tetraamino-4*H*,4′*H*-[3,3′-bi(1,2,4-triazol)]-1-ium, and 3,9-diamino-6,7-dihydro-5*H*-bis([1,2,4]triazolo)[4,3-*e*:3′,4′-*g*][1,2,4,5]tetrazepine-2,10-diium ($C_5H_{10}N_{10}^{2+}$) pentazolate [66, 67], can be obtained *via* metathesis reactions using sodium pentazolate $[Na(H_2O)(N_5)]\cdot 2H_2O$ [32] and the corresponding chlorides, respectively, can be considered, where the reaction is driven by the low solubility of sodium chloride (Figure 1.23). Among them, 4,4′,5,5′-tetraamino-4*H*,4′*H*-[3,3′-bi(1,2,4-triazol)]-1-ium pentazolate·$3H_2O$ ($(C_4H_9N_{10}^+)(N_5^-)\cdot 3H_2O$, **1-17**) and $(C_5H_9N_{10}^+)_2(Cl^-)(N_5^-)\cdot 3.5H_2O$ (**1-18**) can be synthesized in one pot.

The $[Na(H_2O)(N_5)]\cdot 2H_2O$ [32] could be transformed into AgN_5 precipitate by reaction with $AgNO_3$ in aqueous solution. Ammonium (**1-20**), hydroxylammonium (**1-21**), hydrazinium (**1-22**), aminoguanidinium (**1-23**), diaminoguanidinium (**1-24**), biguanidinium (**1-25**), 3,4-diamino-1,2,4-triazolium (**1-26**), and 3,6,7-triamino-7*H*-[1,2,4]triazolo[4,3-*b*][1,2,4]triazol-2-ium (**1-27**) pentazolates were synthesized by metathesis reactions of AgN_5 with stoichiometric amounts of the respective chloride salts [51] (Figure 1.24). The metathesis reactions were driven by the precipitation of AgCl, which has a very low solubility in water. So, high yields (>90%) of target pentazolate salts can be obtained by simple filtration followed by the concentration of the filtrate.

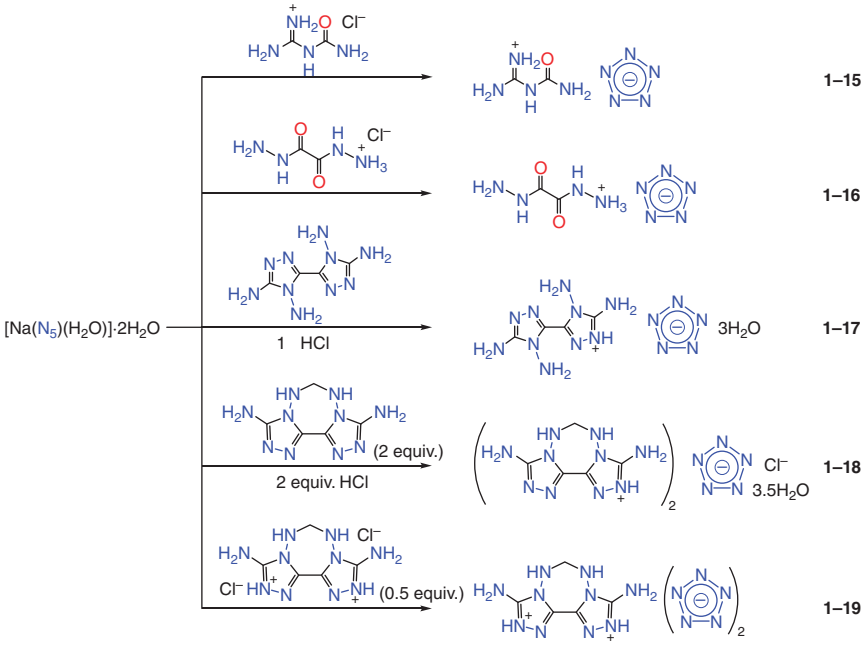

Figure 1.23 Synthesis of compounds **1-15** to **1-19**.

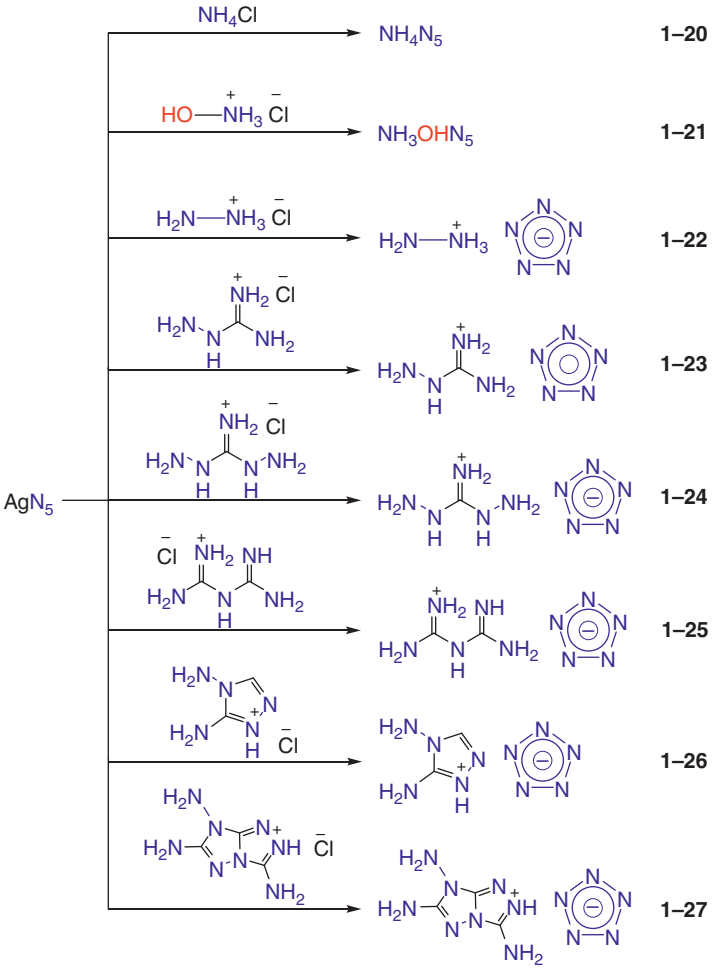

Figure 1.24 Synthesis of compounds **1-20** to **1-27**.

1.5.2 Single-Crystal X-Ray Structures

Salt **1-15** ($C_2H_7N_9O$) crystallizes in the monoclinic $P2_1/c$ space group with four molecules in the unit cell (Figure 1.25). Its calculated density is 1.596 g cm^{-3} at 173 K. As shown in Figure 1.25, the *N*-carbamoylguanidinium cation together with *cyclo*-N_5^- anion is approximately in the plane, which can be seen from the torsion angle C1–C2–N5–N1 of 0.43° and N4–N1–N5–N2 of 0.2°. The C—N bond lengths and the N—C—N bond angles in the *N*-carbamoylguanidinium cation are in the range of 1.313(2)–1.356(2) and 113.20(14)–126.22(16) Å, respectively, which are typical values for the *N*-carbamoylguanidinium cation [68]. The N—N bond lengths in the *cyclo*-N_5^- are in the range of 1.299(2)–1.335(2) Å, with an average N—N bond distance of 1.318 Å, which is similar to that of $[Na(H_2O)(N_5)]\cdot 2H_2O$ (1.316 Å), $[Mg(H_2O)_6(N_5)_2]\cdot 4H_2O$ (1.316 Å), and $[Mn(H_2O)_4(N_5)_2]\cdot 4H_2O$ (1.320 Å). Since the

Figure 1.25 Crystal structure of salt **1-15**.

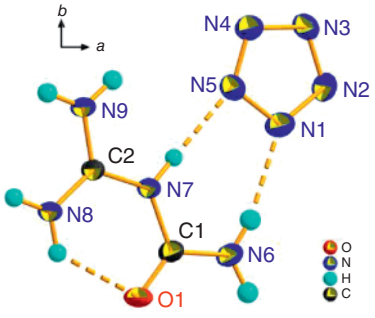

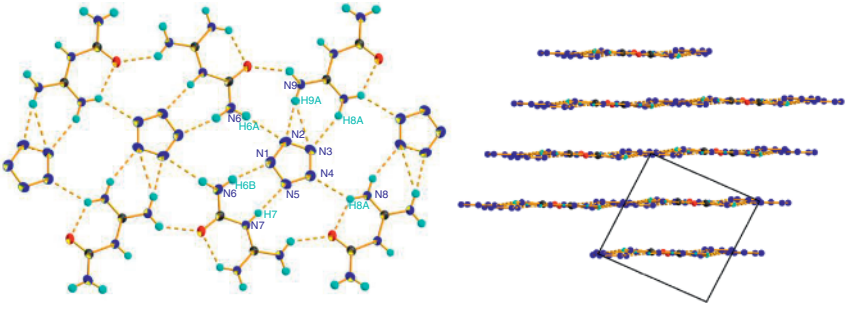

(a) (b)

Figure 1.26 (a) 2D layered intermolecular interactions in the crystal structure of salt **1-15**; (b) 3D structural layer network in salt **1-15**.

amino groups in *N*-carbamoylguanidinium are excellent hydrogen-bonding donors, the discrete *cyclo*-N_5^- rings are linked into a stable 2D layer by the hydrogen-bonding interactions between cations and anions (Figure 1.26). The face-to-face stacking of **1-15** shows that there are no significant interactions between adjacent layers.

Salt **1-16** ($C_2H_7N_9O_2$) crystallizes in the same space group (monoclinic $P2_1/c$) with **1-15** and eight molecules in the unit cell (Figure 1.27). Its crystal density (1.681 g cm^{-3} at 173 K) is higher than that of **1-15**. Two forms of *cyclo*-N_5^- can be found in **1-16**, with the N—N bond lengths in the range of 1.294(5)–1.339(5)

Figure 1.27 Crystal structure of **1-16**.

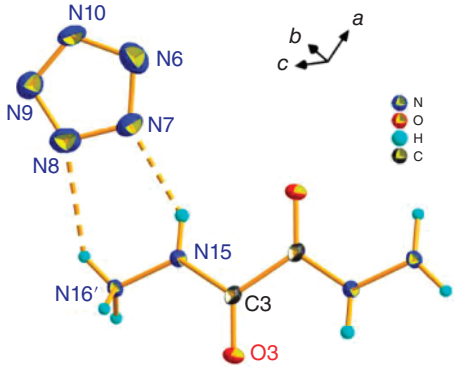

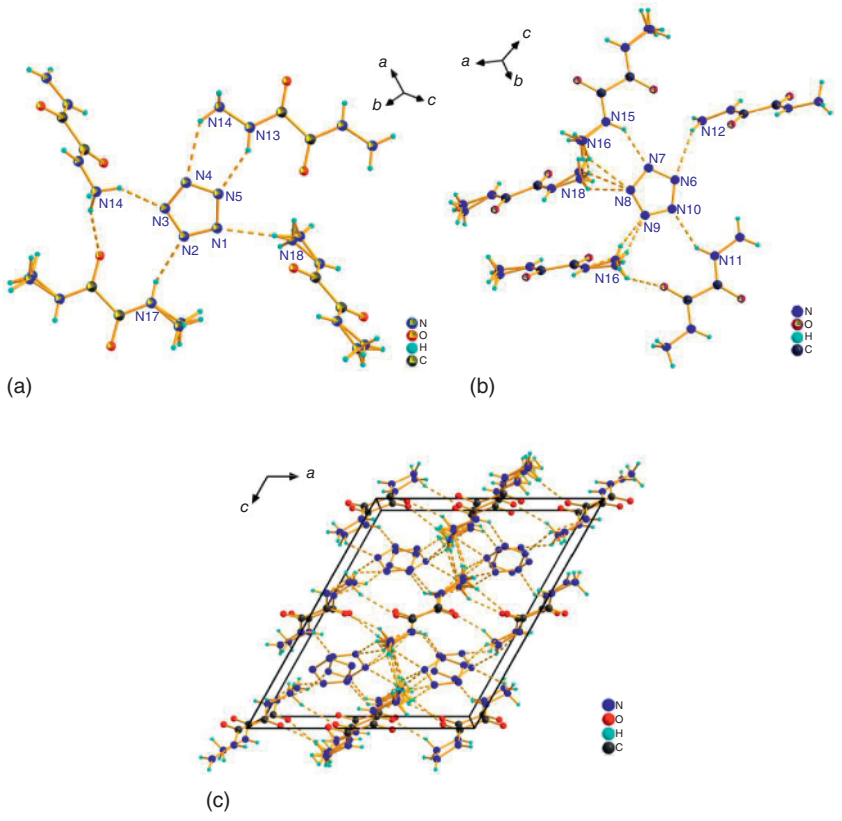

Figure 1.28 (a, b) The hydrogen bonds of *cyclo*-N_5^- in **1-16**; (c) A view of the packing down the *b*-axis of the unit cell of **1-16**. Dashed lines indicate strong hydrogen bonding.

and 1.301(5)–1.333(5) Å and the largest torsion angle N2–N1–N5–N4 of 0.64° and N10–N6–N7–N8 of 1.31°. Every *cyclo*-N_5^- ring participates in at least five hydrogen bonds (Figure 1.28). The lengths of the hydrogen bonds are shorter than the sum of the van der Waals radii (r_w(N) + r_w(N) = 3.20 Å); thus, a strong hydrogen-bond network is formed.

Salt **1-17** ($C_4H_{15}N_{15}O_3$) crystallizes in the triclinic space group *P*-1 with a density of 1.520 g cm^{-3} at 173 K (Figure 1.29). Unlike most complexes, the *cyclo*-N_5^- ring in **1-17** lacks perfect planarity, with the largest torsion angle (N13–N11–N12–N15) of 0.64° which is shorter than that of $[Mg(H_2O)_6(N_5)_2]\cdot 4H_2O$ (0.85°) [32]. We can see from Figure 1.30 that the crystal is layer by layer stacked and the interlayer distance is 3.42 Å. The adjacent layers are connected by two kinds of hydrogen bonds (O2—O3 HBs and O1—N1 HBs).

Salt **1-18** crystallizes from water in the triclinic space group *P*-1 with a density of 1.617 g cm^{-3} at 173 K and four fused $C_5H_9N_{10}^+$ cations, two Cl^-, two *cyclo*-N_5^-, and seven water moieties per unit cell (Figures 1.31 and 1.32). The N—N bond lengths (1.390(3) and 1.396(3) Å) of the unprotonated 1,2,4-triazoles are slightly longer than those of the protonated triazoles (1.382(3) Å). All the amino groups participate in

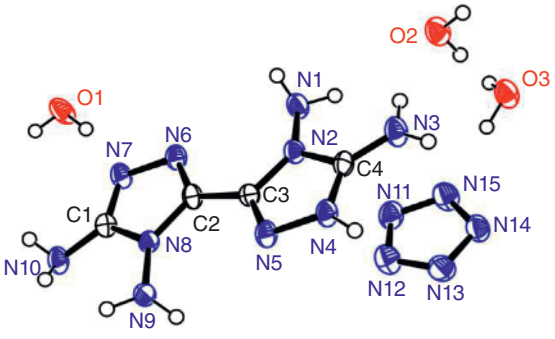

Figure 1.29 Crystal structure of **1-17**.

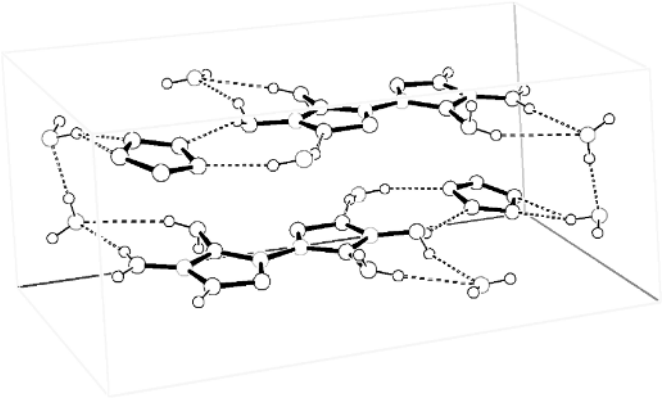

Figure 1.30 The 3D structure of **1-17** constructed by hydrogen-bonding networks.

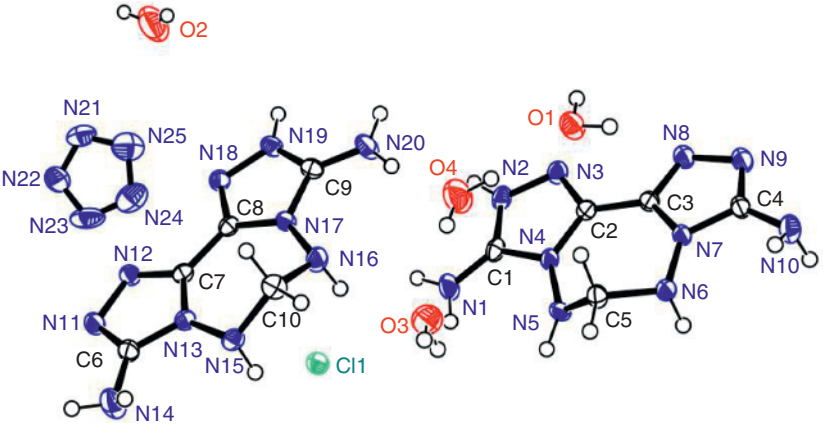

Figure 1.31 Crystal structure of **1-18**.

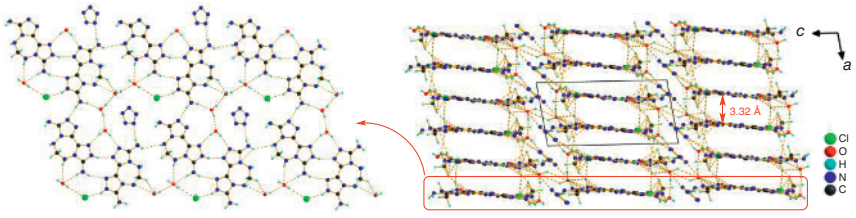

Figure 1.32 The 3D structure of **1-18** constructed by hydrogen-bonding networks.

hydrogen bonds and act as donors, whereas in the two fused cations only N3, N9, N11, N12, and N18 act as hydrogen-bond acceptors. Numerous hydrogen bonds around *cyclo*-N_5^- can be seen from the *b*-axis (*ac* plane) of the packing diagram. The interlayer distance in **1-18** is 3.32 Å, which is slightly shorter than that of **1-17** (3.42 Å).

Salt **1-19** crystallizes in the monoclinic space group *C*2/*c* with a density of 1.660 g cm^{-3} at 173 K and four molecules in the unit cell (Figure 1.33). The cation DABTT^{2+} exhibits a trans structure with an angle of 36.68° between two amino-triazole planes (Figure 1.34). The C3—N5 bond length of C-amino

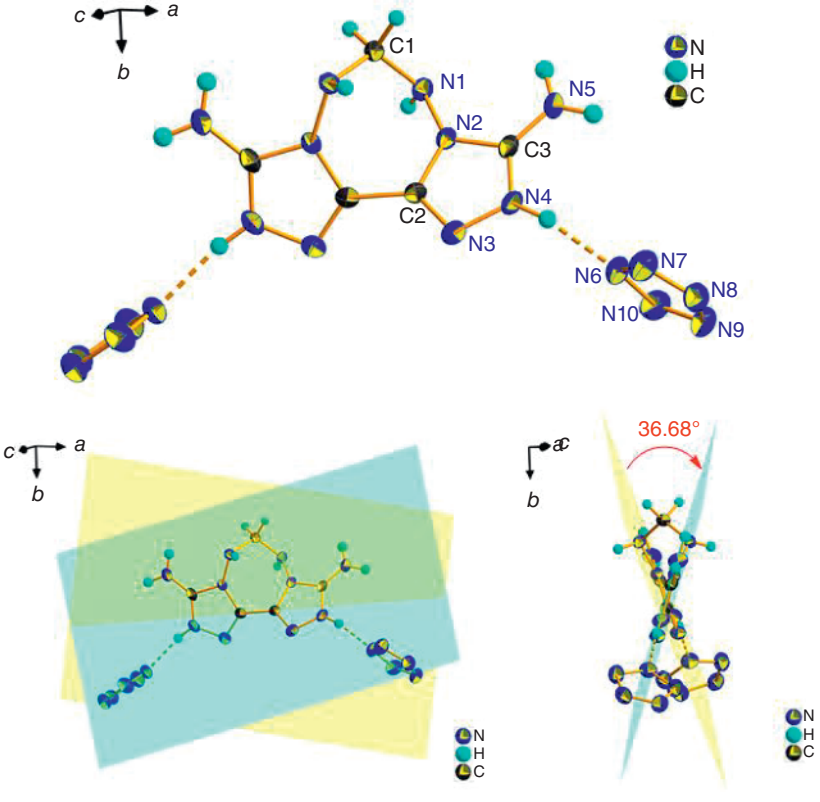

Figure 1.33 Crystal structure of **1-19**.

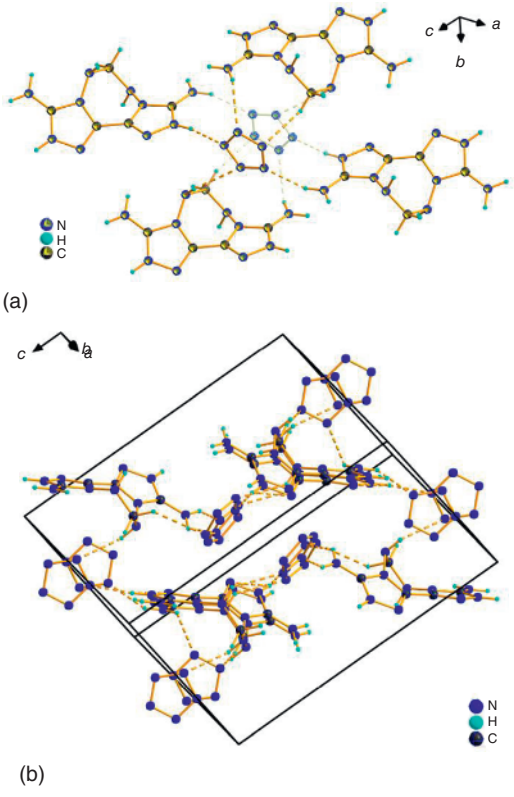

Figure 1.34 (a) The hydrogen bonds of *cyclo*-N_5^- in **1-19**; (b) A view of the packing of the unit cell of **1-19**.

group is 1.313(2) Å, which is slightly shorter than three C—N bonds (C2—N2: 1.379(2) Å; C3—N2: 1.3558(19) Å; C3—N4: 1.334(2) Å) and longer than one C—N bond (C2—N3: 1.291(2) Å) of the triazole moiety. With the bond lengths of 1.291(2)–1.385(2) Å, the distances between the ring atoms of the triazole moiety lie between the length of formal C—N and N—N single and double bonds, which indicates the aromaticity of the ring system [69].

Salt **1-20** crystallizes in the orthorhombic *Pcca* space group with four molecules per unit cell (Figures 1.35 and 1.36). The N—N bond lengths for *cyclo*-N_5^- in **1-20** are 1.309(2), 1.309(2), 1.316(2), 1.316(2), and 1.316(3) Å; the average N—N bond distance (1.3132 Å) is shorter than that of most reported metal-N_5^- compounds (1.314–1.329 Å). The structure of the *cyclo*-N_5^- in **1-20** is almost planar ($N3^{ii}$–N3–N2–N1 = 0.02°, N2–$N2^{ii}$–N1–$N3^{ii}$ = 0.01°). All hydrogenated

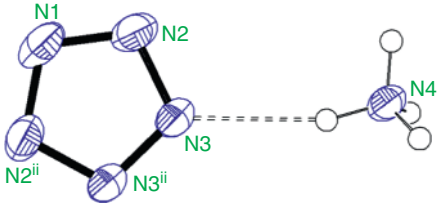

Figure 1.35 Crystal structure of salt **1-20**.

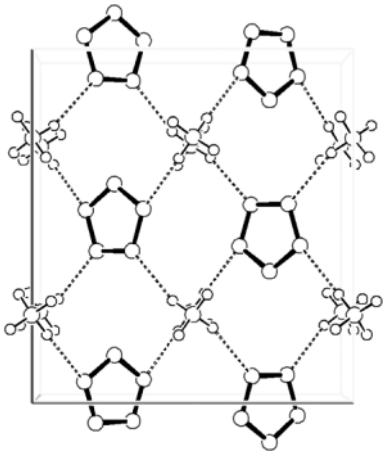

Figure 1.36 Ball-and-stick packing diagram of **1-20** viewed down the *b* axis.

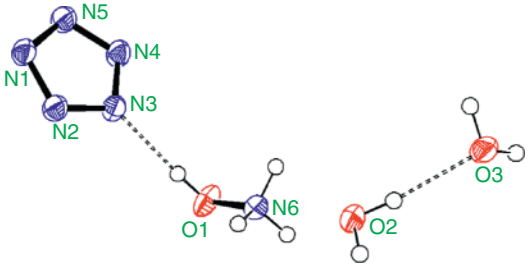

Figure 1.37 Crystal structure of **1-21**·$2H_2O$.

nitrogen atoms (N4) participating in hydrogen bonds act as donors, while only four nitrogen atoms (except for N1) of each *cyclo*-N_5^- act as hydrogen-bond acceptors.

Both **1-21**·$2H_2O$ and **1-22** crystallize in the monoclinic $P121/c1$ space group with four molecules per unit cell (Figures 1.37–1.40). The average N—N bond distances in **1-21**·$2H_2O$ and **1-22** are 1.3152 and 1.3227 Å, which are slightly longer than that of **1-20**. Unlike **1-20**, the five nitrogen atoms of *cyclo*-N_5^- in **1-21**·$2H_2O$ and **1-22** are all not completely coplanar, which could be seen from the largest torsion angle of 0.29°

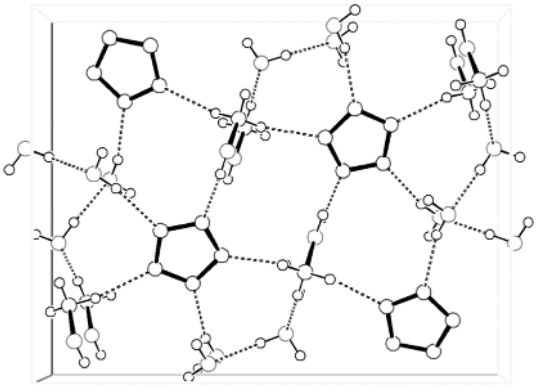

Figure 1.38 Ball-and-stick packing diagram of **1-21**·$2H_2O$.

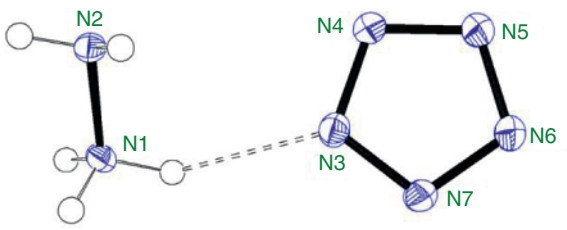

Figure 1.39 Crystal structure of **1-22**.

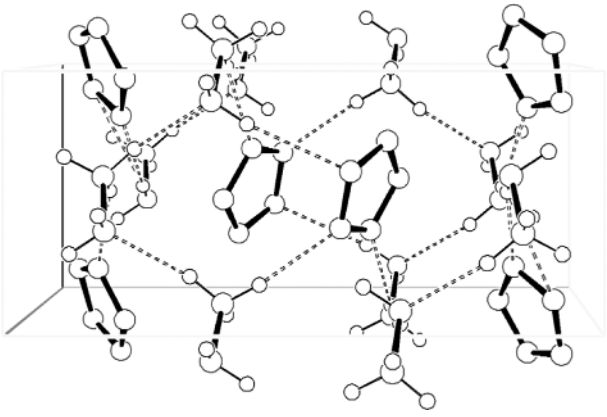

Figure 1.40 Ball-and-stick packing diagram of **1-22**.

(N3–N4–N5–N1) for **1-21**·$2H_2O$ and 0.45° (N5–N7–N6–N3) for **1-22**. All nitrogen atoms of *cyclo*-N_5^- in **1-21**·$2H_2O$ and **1-22** act only as hydrogen-bond acceptors. The N6 and O1 atoms of hydroxylammonium cations act only as donors, while the hydrazinium cations act as not only donors (N1) but also acceptors (N2). Thus, it is not surprising that the *cyclo*-N_5^- anions are controlled by extensive hydrogen-bond networks.

Salt **1-23** crystallizes in the monoclinic $P121/n1$ space group with four molecules per unit cell ($Z = 4$) and a calculated density of 1.476 g cm^{-3} at 150 K (Figure 1.41). The aminoguanidinium cations and the corresponding *cyclo*-N_5^- anions are coplanar with torsion angles of 11.777° (N4–N3–N6–N7), 7.480° (N8–N2–N7–N1), and 10.077° (N6–N3–N2–N1). In addition, a large number of hydrogen bonds between aminoguanidinium cations and *cyclo*-N_5^- anions form a 2D layer (Figure 1.42). Salt **1-23** is layer-by-layer stacking and the interlayer distance is 3.18 Å. The adjacent layers are connected by two kinds of hydrogen bonds (N9–H9A…N5 and NH9–H9B…N3).

Salt **1-24** crystallizes in the triclinic *P*-1 space group with two molecules per unit cell and a calculated density of 1.465 g cm^{-3} at 173 K (Figures 1.43 and 1.44). The diaminoguanidinium cation in **1-24** is almost planar with the torsion angles of 3.49° (N10–N8–C1–N9), 14.45° (N10–C1–N7–N6), and 0.05° (N9–N6–N7–N8). Unlike **1-23**, the diaminoguanidinium cations are not coplanar with the *cyclo*-N_5^- rings, they are almost perpendicular to each other with an angle of 79.657°. In addition to hydrogen bonds between *cyclo*-N_5^- and cations, strong intramolecular hydrogen

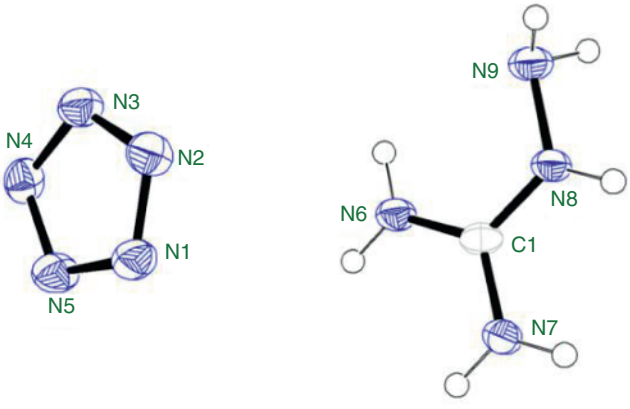

Figure 1.41 Crystal structure of **1-23**.

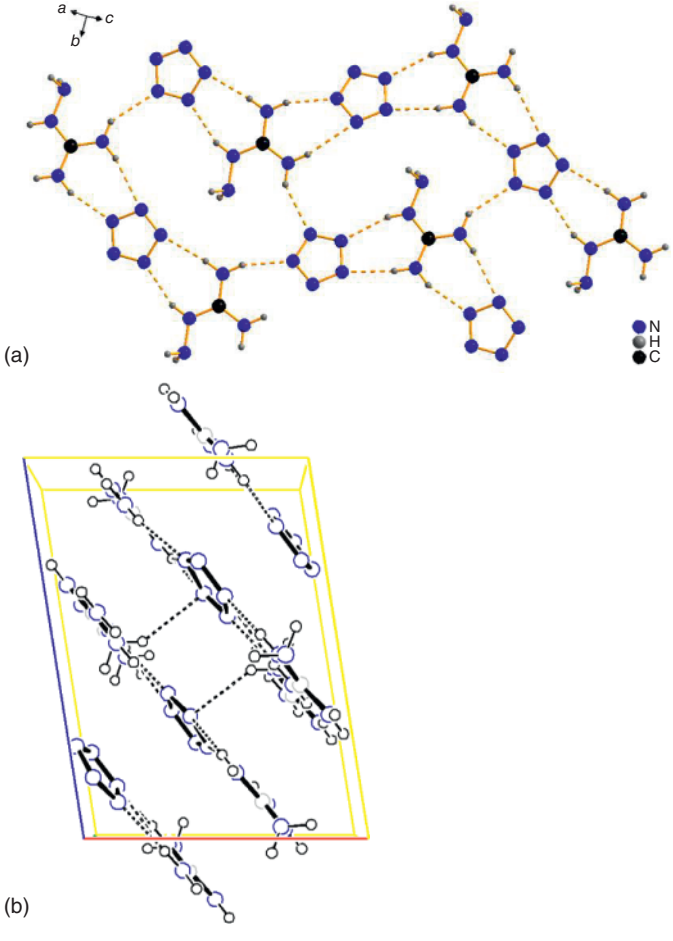

Figure 1.42 (a) Hydrogen bonds in **1-23**; (b) Ball-and-stick packing diagram of **1-23**.

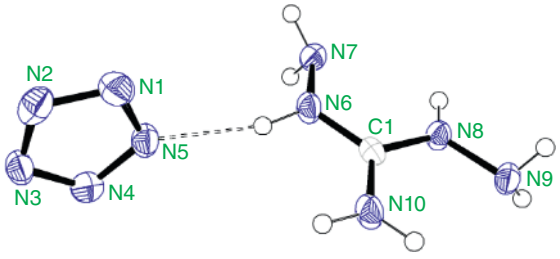

Figure 1.43 Crystal structure of **1-24**.

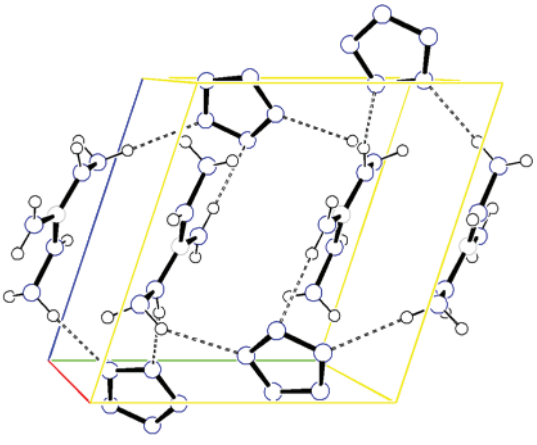

Figure 1.44 Ball-and-stick packing diagram of **1-24**.

bonds (N8—H8…N7 = 2.6856 Å; N10—H10A…N9 = 2.6536 Å) are present in each cation.

Salt **1-25** crystallizes in the monoclinic $P121/c1$ space group with four molecules per unit cell ($Z = 4$) (Figures 1.45 and 1.46). It has a higher calculated density of 1.524 g cm^{-3} (150 K) than **1-23** and **1-24**. The crystal structure of biguanidinium cation in **1-25** does not show hydrogen on the bridging nitrogen (N8), which is consistent with the literature [70]. The biguanidinium cation cannot maintain a planar structure due to the steric hindrance of two adjacent amino groups (N7 and N10). The dihedral angle between plane through N6, N7, N8 and plane through

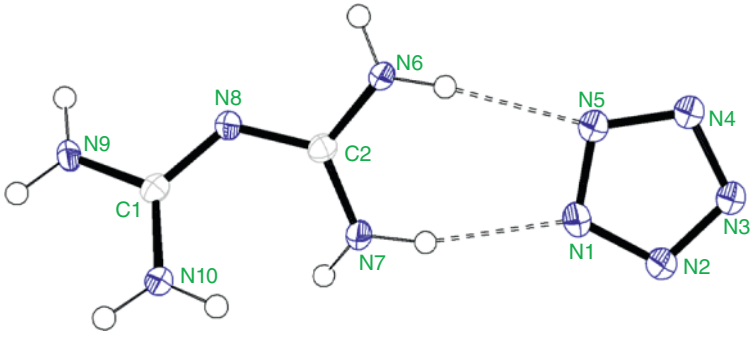

Figure 1.45 Crystal structure of **1-25**.

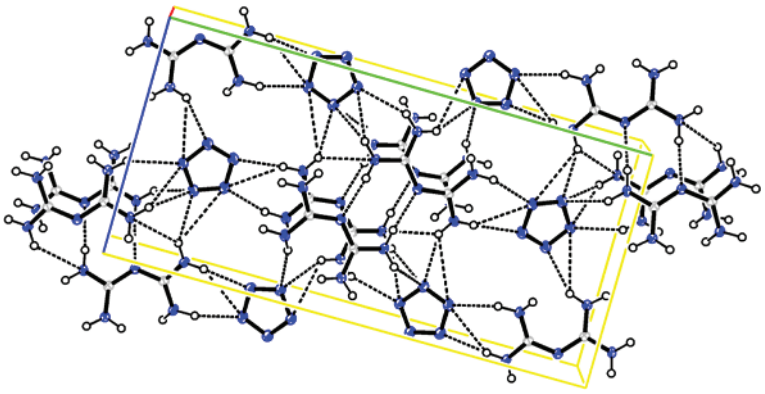

Figure 1.46 Ball-and-stick packing diagram of **1-25**.

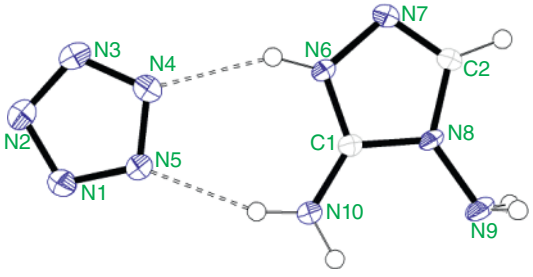

Figure 1.47 Crystal structure of **1-26**.

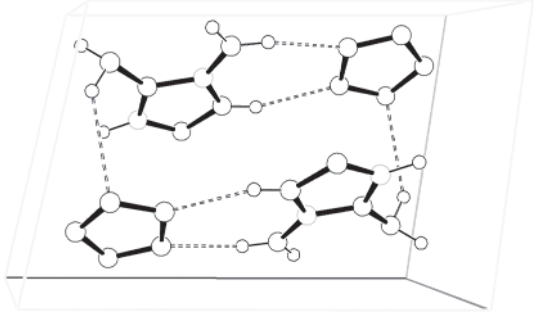

Figure 1.48 Ball-and-stick packing diagram of **1-26**.

N8, N9, N10 is 33.042°. Each biguanidinium cation is substantially coplanar with one of the two *cyclo*-N_5^- rings adjacent thereto which could be seen from the N6–N1–N5–N7 torsion angle of 4.39°.

Salt **1-26** crystallizes in the triclinic *P*-1 space group with two molecules per unit cell and has a calculated density of 1.618 g cm^{-3} (173 K) (Figure 1.47). As shown in Figure 1.48, all carbon and nitrogen atoms and most hydrogen atoms lie in the same plane as supported by the N10—H10A…N5 (2.958(3) Å) and N6—H6…N4 (2.956(3) Å) hydrogen bonds to form a unit. The distance between two adjacent planar units is 3.19 Å.

Salt **1-27** (Figures 1.49 and 1.50) is described by the monoclinic space group *P*121/*c*1 with a density of 1.645 g cm^{-3} at 173 K and four molecules per unit cell.

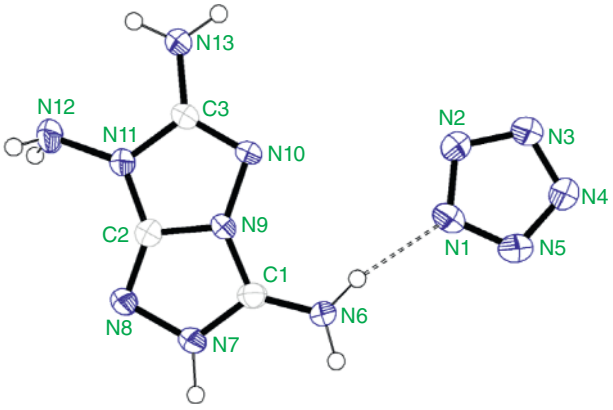

Figure 1.49 Crystal structure of **1-27**.

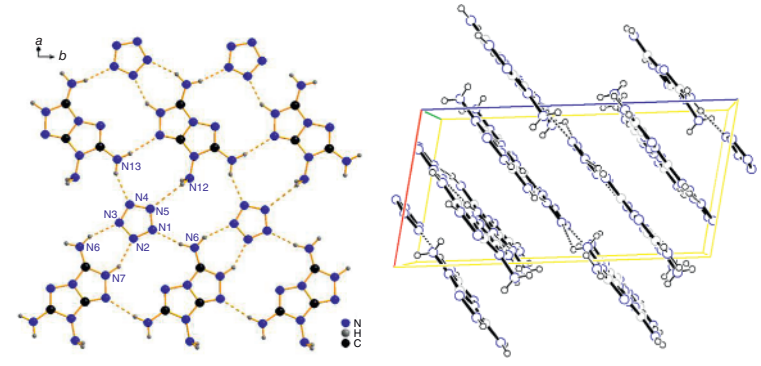

(a) (b)

Figure 1.50 (a) Hydrogen bonds in **1-27**; (b) Ball-and-stick packing diagram of **1-27**.

Every *cyclo*-N_5^- ring participates in five hydrogen bonds to form a 2D layer. We can see from Figure 1.10b that **1-27** is layer-by-layer stacking and the interlayer distance is 3.01 Å which is shorter than that of **1-23** (3.18 Å).

1.5.3 Properties

1.5.3.1 ^{15}N NMR

The ^{15}N NMR spectrum of salt **1-15** was measured in dimethyl sulfoxide (DMSO)-D_6 with respect to CH_3NO_2 as an external standard. Nitrogen signals were assigned based on the literature [68] and Giao NMR calculation with Gaussian 09 [71]. As shown in Figure 1.51, the nitrogen atoms of *cyclo*-N_5^- (N1) resonate at −5.95 ppm, consistent with the $[Na(H_2O)(N_5)]\cdot 2H_2O$ (−5.7 ppm) [32]. Apart from the signal of the *cyclo*-N_5^- anion, the three kinds of hydrogen-attached nitrogen atoms have higher negative resonances. The N2 nitrogen atom (NH) resonates at the lowest field of all three at −269.19 ppm, whereas the two different kinds of NH_2 groups have very similar shifts at −291.28 ppm (N3) and −296.49 ppm (N4). In

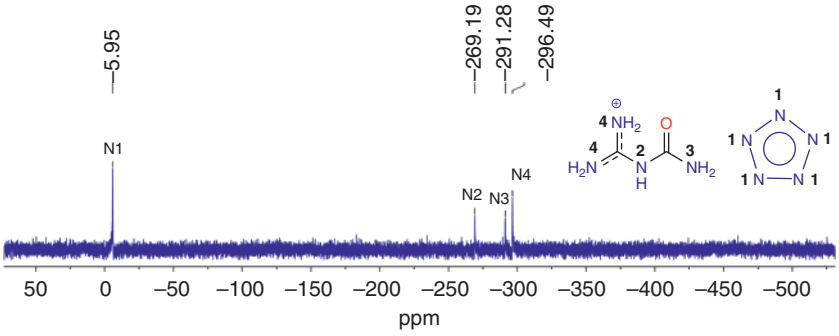

Figure 1.51 ^{15}N NMR spectrum of salt **1-15**.

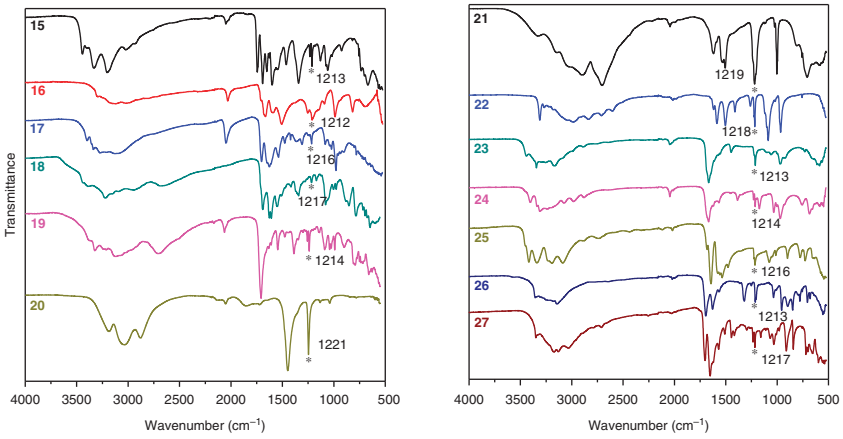

Figure 1.52 IR spectra of **1-15**–**1-20** to **1-21**–**1-27**.

contrast to the spectrum of *N*-carbamoylguanidinium nitrate [68], the signals for the cation (N2, N3, and N4) were shifted about 2 ppm to lower fields.

1.5.3.2 IR Spectrum

In the IR spectra (Figure 1.52), the strong *cyclo*-N_5^- bands were found at 1213–1221 cm^{-1}, which are red-shifted by about 20 cm^{-1} than metal salts $[Na(H_2O)(N_5)]\cdot 2H_2O$, $[M(H_2O)_4(N_5)_2]\cdot 4H_2O$ (M = Mn, Fe, Co, and Zn), and $[Mg(H_2O)_6(N_5)_2]\cdot 4H_2O$ [32, 47]. The stretching vibration of the N—H bonds is observed between 3500 and 3000 cm^{-1}. The strongest band observed in the IR spectra of **1-15**, **1-17** to **1-19**, **1-23** to **1-27** is the C=N stretch at 1667, 1668, 1644, 1629, and 1652 cm^{-1}, respectively. In addition, many combined stretching and deformation as well as torsion stretching modes could be observed in the fingerprint region between 1000 and 500 cm^{-1}.

1.5.3.3 Thermal Stability

The thermal stability of *cyclo*-N_5^- based compounds has long been an important concern by chemists. Here, TG and DSC of **1-15** to **1-27** were carried out to

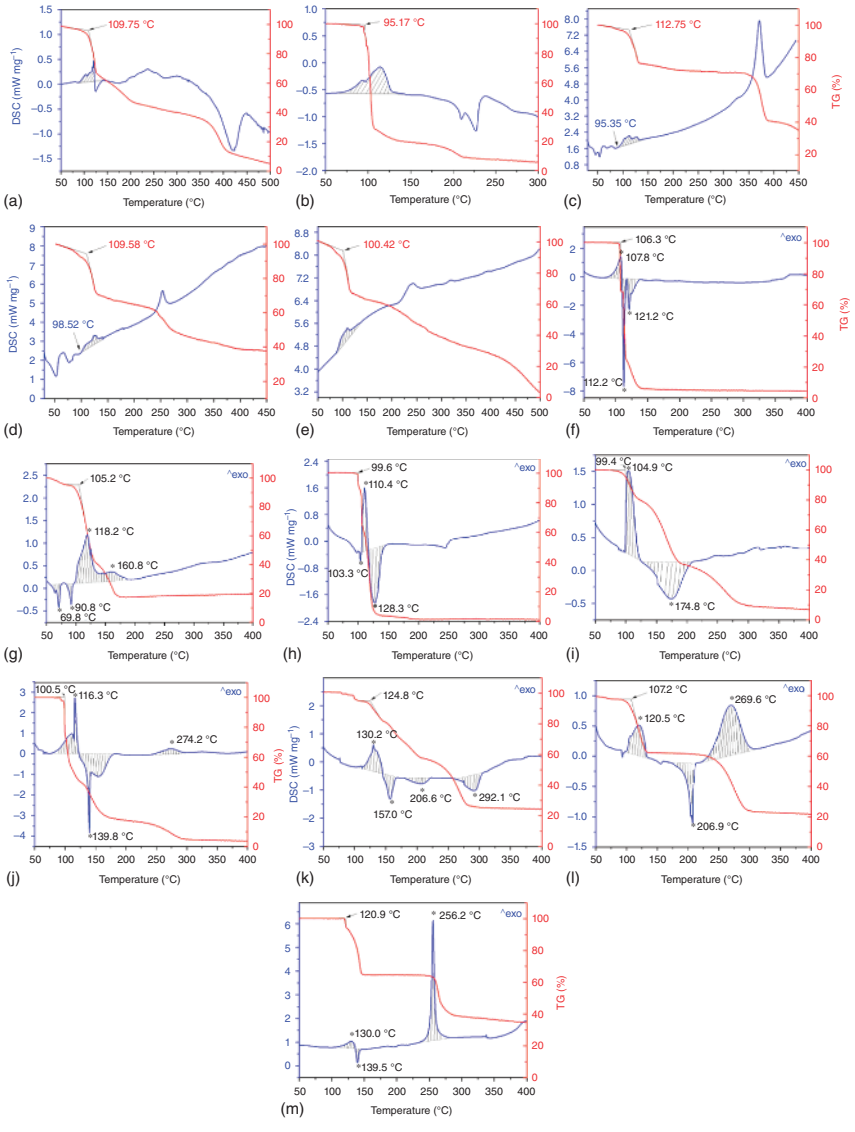

Figure 1.53 DSC and TG of salts **1-15** to **1-27**.

determine their thermal behaviors at a heating rate of 5 °C min^{-1}. As shown in Figure 1.53, the *cyclo*-N_5^- based compounds all decomposed without melting. The *cyclo*-N_5^- rings in the nonmetallic salts are decomposed into N_3^- and N_2 at about 100 °C. For most salts, the exothermic peak of each compound follows an obvious endothermic peak which should be caused by the volatilization of hydrazoic acid (HN_3).

The onset decomposition temperatures (T_d) taken from their TG curves indicate that these salts have good thermal stabilities (T_d > 95.2 °C). In addition to

compounds **1-16**, **1-22**, and **1-23**, other new synthesized *cyclo*-N_5^- based salts have decomposition temperatures above 100 °C. Especially, salts **1-25** and **1-27** show excellent thermal stabilities with onset decomposition temperatures of 124.8 and 120.9 °C, respectively. After the decomposition of the *cyclo*-N_5^-, their weight loss processes depend on the type of counter cations: when the cations are simple and carbon-free ammonium, hydroxylammonium, and hydrazinium, the TG curves show significant weight losses in a narrow range from 90 to 170 °C; when the cations are guanidinium, triazolium, and fused cations, the TG curves show obvious weight losses in a relatively wider range from 90 to 300 °C.

1.5.3.4 Sensitivity

For safety purposes, the sensitivities toward impact (IS) and friction (FS) were measured by using standard BAM methods [72]. Salts **1-16** and **1-21** are the most impact and friction-sensitive energetic materials (IS = 6 and 5.5 J, FS = 80 and 50 N) among these *cyclo*-N_5^- compounds. The impact and friction sensitivities of salts **1-15**, **1-19**, **1-20**, and **1-22** are measured to be 7.4–14 and 7.4 J, 120–160 N, respectively, which are comparable with those of RDX and HMX (IS = 7.4 J, FS = 120 N). Salts **1-24** and **1-25** are less impact and friction sensitivities with IS values of 25 and 30 J and FS values of 240 and 300 N, which are comparable with FOX-12 (IS = 30 J, FS = 350 N). Salts **1-23**, **1-26**, and **1-27** were determined to be insensitive to impact and friction (IS > 40 J, FS = 120 N), which highlight their likely application potential as insensitive energetic materials.

With respect to Hirshfeld surfaces (Figure 1.54), salts **1-23**, **1-26**, and **1-27** appear in plate shapes, which indicate insensitivity as it represents planar conjugated molecular structures. And their red dots (predominant intermolecular interactions) are located on the surface edges; in this way, the layers are supported by π–π stacking and thus sustain the maximum external *stimuli*.

1.5.3.5 Density

The densities of these salts fall between 1.312 and 1.650 g cm^{-3} (Table 1.4), less than those of the predicted polynitrogen compounds (2.0–3.9 g cm^{-3}) and TNT (1.65 g cm^{-3}). Fused triazolium pentazolates (**1-19** and **1-27**) have higher densities than other structures. Monocyclic triazolium pentazolate has a lower density than fused triazolium pentazolates. In addition, comparing compounds **1-15** and **1-25**, we found that oxygen-containing cations are beneficial to increase the density of the pentazolate salts.

1.5.3.6 Heat of Formation and Detonation Performance

The solid-phase heats of formation for **1-15** to **1-27** are calculated using the gas phase heat of formation and heat of phase transition (lattice energy) according to Hess's law of constant summation [73] (Born–Haber energy cycle). The heats of formation of *cyclo*-N_5^- anion and most cations involved in the calculations are referenced from the literature [58, 74, 75]. Others were calculated by the Gaussian 09 (Revision A.02) suite of programs [71]. Except for pentazolate salts containing crystal water and Cl^-, all the *cyclo*-N_5^- based energetic salts have relatively high positive heats of formation

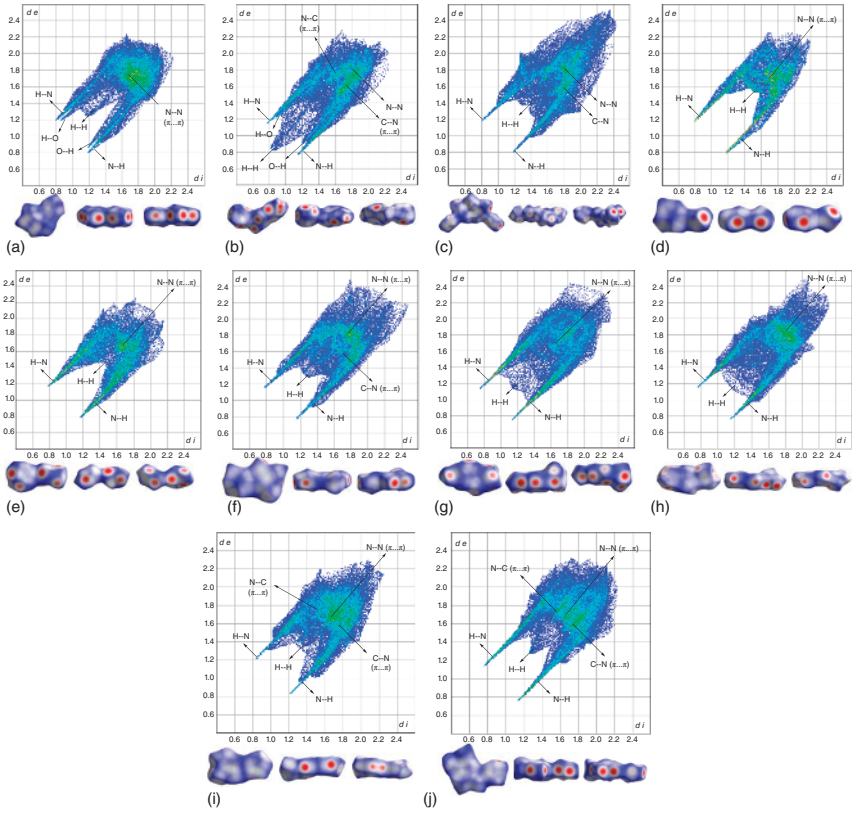

Figure 1.54 Two-dimensional fingerprint plots and Hirshfeld surfaces for **1-15** (a), **1-16** (b), **1-19** (c), **1-20** (d), and **1-22** to **1-27** (e–j).

(ΔH_f) falling between 203.4 (**1-15**) to 1362.0 (**1-25**) kJ mol^{-1} (Table 1.4), which exceed TNT (−67 kJ mol^{-1}), RDX (80 kJ mol^{-1}), and HMX (104.8 kJ mol^{-1}). Among them, the biguanidinium salt **1-25** has the highest heat of formation (1362.0 kJ mol^{-1}) due to the very high heat of formation of biguanidinium cation (1618 kJ mol^{-1}). Therefore, the incorporation of a cation with high heat of formation can still be considered as a useful way to increase the heat of formation of a *cyclo*-N_5^- based energetic ion salt.

The detonation performances of these salts were calculated using the EXPLO5 program (version 6.01) [76] based on the calculated heats of formation and densities at ambient temperature. The calculated detonation velocity (D) and pressure (P) values (Table 1.4) fall in the range of 6920–9257 m s^{-1} and 18.9–33.0 GPa, respectively, which are higher than those of TNT (6.881 km s^{-1}, 19.5 GPa). With respect to D, the values of **1-22** and **1-21** (8796 and 9005 m s^{-1}) exceed FOX-12 and RDX (8323 and 8795 m s^{-1}) and salt **1-25** remarkably exceeds those values at 9257 m s^{-1}, which is higher than HMX (9144 m s^{-1}). In terms of P, the values for **1-21**, **1-22**, and **1-25** (32.7, 30.8, 33.0 GPa) are higher than those of FOX-12 (26.6 GPa) and comparable with those of RDX (34.9 GPa).

Table 1.4 Physicochemical and energetic properties of **1-15** to **1-27**, RDX, HMX, and FOX-12.

Compound	ρ[a] (g cm^{-3})	ΔH_f[b] (kJ mol^{-1}/ kJ g^{-1})	D[c] (m s^{-1})	P[d] (GPa)	IS[e] (J)	FS[f] (N)	OB[g] (%)	N[h] (%)
1-15	1.567/ 1.596(173 K)	203.4/ 1.18	6920	18.9	14	160	−41.6	72.81
1-16	1.650/ 1.681(173 K)	388.1/ 2.05	8320	27.1	6	80	−29.6	66.65
1-17	1.492/ 1.520(173 K)	—	—	—	—	—	—	65.40
1-18	1.587/ 1.617(173 K)	—	—	—	—	—	—	59.66
1-19	1.629/ 1.660(173 K)	1341.2/ 3.83	7615	23.6	10	120	−45.7	79.98
1-20	1.486/ 1.519(150 K)	269.1/ 3.06	7757	23.2	8	130	−36.4	95.42
1-21	1.601/ 1.636(153 K)	327.6/ 3.15	9005	32.7	5.5	50	−15.4	80.75
1-22	1.583/ 1.618(150 K)	429.6/ 4.17	8796	30.8	7.4	120	−38.8	95.11
1-23	1.444/ 1.476(150 K)	392.1/ 2.70	7189	19.6	>40	>360	−49.7	86.86
1-24	1.438/ 1.465(173 K)	508.0/ 3.17	7505	21.2	25	240	−50.0	87.46
1-25	1.491/ 1.524(150 K)	1362.0/ 7.91	9257	33.0	35	300	−55.8	81.36
1-26	1.583/ 1.618(150 K)	639.7/ 3.76	7824	24.5	>40	>360	−47.06	82.33
1-27	1.615/ 1.645(173 K)	853.8/ 3.79	7791	24.6	>40	>360	−46.2	80.86
RDX	1.806	80.0/ 0.36	8795	34.9	7.4	120	0	37.84
HMX	1.905	74.8/ 0.25	9144	39.2	7.4	120	0	37.84
FOX-12	1.754	−355.0/ −1.59	8323	26.6	30	350	−3.8	46.89

a) Density, recalculated from low-temperature X-ray densities $\{\rho_{298K} = \rho_T/[1 + 1.5 \times 10^{-4} (298 - T)]\}$. Values after slashes are crystal densities.
b) Heat of formation calculated in solid state.
c) Detonation velocity calculated by EXPLO5 V6.01.
d) Detonation pressure calculated by EXPLO5 V6.01.
e) Impact sensitivity.
f) Friction sensitivity.
g) Oxygen balance (based on CO) for $C_aH_bO_cN_d$, $1600(c - a - b/2)/M_w$; M_w = molecular weight.
h) Nitrogen content.

1.6 Conclusions

In summary, a comprehensive overview of the chemistry and performance of the pentazole-based energetic materials was performed. It should be emphasized that the pentazole chemistry is a rather new area of research and all presented data correspond to the twenty-first century. Long-term computational investigations revealed a high heat of formation of the pentazole ring and demonstrated a huge potential of pentazole derivatives as desirable high-energy compounds. Recent synthetic efforts provided reliable routes to the preparation of various pentazoles including their metal-free and metal-containing derivatives. Multidisciplinary investigations of functional properties of pentazolate-derived ionic compounds showed their application potential both as primary explosives and as components of energetic formulations. Importantly, such compounds have a high level of environmental compatibility, due to the presence of the fully nitrogen heterocyclic core, which upon detonation releases molecular nitrogen as a main decomposition product. There is no doubt that investigations on pentazole-based energetic materials will be of increased attention in near future and should be an excellent platform for the development of novel advanced energetic materials.

References

1 Klapötke, T.M. (2012). *Chemistry of High-Energy Materials*, vol. 2. Berlin: De Gruyter.
2 Christe, K.O. (2007). *Propellants Explos. Pyrotech.* 32: 194–204.
3 Nguyen, M.T., McGinn, M.A., Hegarty, A.F., and Elguéro, J. (1985). *Polyhedron* 4: 1721–1726.
4 Nguyen, M.T. (2003). *Coord. Chem. Rev.* 244: 93–113.
5 Dixon, D.A., Feller, D., Christe, K.O. et al. (2004). *J. Am. Chem. Soc.* 126: 834–843.
6 Klapötke, T.M. and Hammerl, A. (2008). *Comprehensive Heterocyclic Chemistry III*, 739–757. Oxford: Elsevier.
7 Vij, A., Pavlovich, J.G., Wilson, W.W. et al. (2002). *Angew. Chem. Int. Ed.* 41: 3051–3054.
8 Huisgen, R. and Ugi, I. (1956). *Angew. Chem.* 68: 705–706.
9 Butler, R.N., Fox, A., Collier, S., and Burke, L.A. (1998). *J. Chem. Soc., Perkin Trans. 2* 2243–2248.
10 Yang, Y., Li, Y., Zhang, R. et al. (2014). *RSC Adv.* 4: 57629–57634.
11 Bondarchuk, S.V. (2020). *J. Phys. Chem. Lett.* 11: 5544–5548.
12 Zhang, X., Yang, J., Lu, M., and Gong, X. (2014). *RSC Adv.* 4: 56095–56101.
13 Zhang, X., Ma, C., Zhang, Y., and Liu, G. (2018). *Struct. Chem.* 29: 267–274.
14 Zhang, X. and Gong, X. (2016). *J. Mol. Model.* 22: 106.
15 Hammerl, A. and Klapötke, T.M. (2002). *Inorg. Chem.* 41: 906–912.
16 Zhang, X., Yang, J., Lu, M., and Gong, X. (2015). *RSC Adv.* 5: 27699–27705.
17 Rahm, M. and Brinck, T. (2010). *Chem. Eur. J.* 16: 6590–6600.

18 Frison, G., Jacob, G., and Ohanessian, G. (2013). *New J. Chem.* 37: 611–618.
19 Liang, Y.H., Luo, Q., Guo, M., and Li, Q.S. (2012). *Dalton Trans.* 41: 12075–12081.
20 Noyman, M., Zilberg, S., and Haas, Y. (2009). *J. Phys. Chem. A* 113: 7376–7382.
21 Yang, J., Gong, X., and Wang, G. (2015). *Struct. Chem.* 26: 1077–1082.
22 Liu, S.J., Zhao, L., Yao, M.G. et al. (2020). *Adv. Sci.* 7.
23 Östmark, H., Wallin, S., Brinck, T. et al. (2003). *Chem. Phys. Lett.* 379: 539–546.
24 Geiger, U., Elyashiv, A., Fraenkel, R. et al. (2013). *Chem. Phys. Lett.* 556: 127–131.
25 Bazanov, B. and Haas, Y. (2015). *J. Phys. Chem. A* 119: 2661–2671.
26 Geiger, U. and Haas, Y. (2015). *J. Phys. Chem. B* 119: 7338–7348.
27 Geiger, U. and Haas, Y. (2016). *J. Phys. Chem. B* 120: 6208–6214.
28 Schroer, T., Haiges, R., Schneider, S., and Christe, K.O. (2005). *Chem. Commun.* 1607–1609.
29 Butler, R.N., Hanniffy, J.M., Stephens, J.C., and Burke, L.A. (2008). *J. Org. Chem.* 73: 1354–1364.
30 Bazanov, B., Geiger, U., Carmieli, R. et al. (2016). *Angew. Chem. Int. Ed.* 55: 13233–13235.
31 Bazanov, B., Geiger, U., Grinstein, D. et al. (2017). *J. Phys. Chem. A* 121: 6727–6731.
32 Xu, Y., Wang, Q., Shen, C. et al. (2017). *Nature* 549: 78–81.
33 Zhang, C., Sun, C., Hu, B. et al. (2017). *Science* 355: 374–376.
34 Christe, K.O. (2017). *Science* 355: 351–351.
35 Yu, T., Ma, Y., Lai, W. et al. (2018). *R. Soc. Open Sci.* 5: 172269.
36 Shang, F.J., Liu, R.Z., Liu, J.Y. et al. (2020). *J. Phys. Chem. Lett.* 11: 1030–1037.
37 Ren, G.H., Liu, R.Z., Zhou, P.W. et al. (2019). *Chem. Commun.* 55: 2628–2631.
38 Steele, B.A. and Oleynik, I.I. (2016). *Chem. Phys. Lett.* 643: 21–26.
39 Steele, B.A., Stavrou, E., Crowhurst, J.C. et al. (2017). *Chem. Mater.* 29: 735–741.
40 Williams, A.S., Steele, B.A., and Oleynik, I.I. (2017). *J. Chem. Phys.* 147: 234701.
41 Laniel, D., Weck, G., Gaiffe, G. et al. (2018). *J. Phys. Chem. Lett.* 9: 1600–1604.
42 Steele, B.A. and Oleynik, I.I. (2017). *J. Phys. Chem. A* 121: 1808–1813.
43 Li, J.F., Sun, L., Wang, X.L. et al. (2018). *J. Phys. Chem. C* 122: 22339–22344.
44 Xia, K., Zheng, X.X., Yuan, J.A. et al. (2019). *J. Phys. Chem. C* 123: 10205–10211.
45 Zhou, M., Sui, M.H., Shi, X.H. et al. (2020). *J. Phys. Chem. C* 124: 11825–11830.
46 Liu, Z., Li, D., Tian, F.B. et al. (2020). *Inorg. Chem.* 59: 8002–8012.
47 Xu, Y., Wang, P., Lin, Q., and Lu, M. (2017). *Dalton Trans.* 46: 14088–14093.
48 Xu, Y., Wang, P., Lin, Q. et al. (2018). *Dalton Trans.* 47: 1398–1401.
49 Zhang, W., Wang, K., Li, J. et al. (2018). *Angew. Chem. Int. Ed.* 57: 2592–2595.
50 Xu, Y., Lin, Q., Wang, P., and Lu, M. (2018). *Chem. Asian J.* 13: 1669–1673.
51 Xu, Y., Tian, L., Li, D. et al. (2019). *J. Mater. Chem. A* 7: 12468.
52 Wang, P., Xu, Y., Lin, Q., and Lu, M. (2018). *Sci. China Mater.* 62: 122–129.
53 Burke, L.A., Butler, R.N., and Stephens, J.C. (2001). *J. Chem. Soc., Perkin Trans. 2* 9: 1679–1684.
54 Tsipis, A.C. and Chaviara, A.T. (2004). *Inorg. Chem.* 43: 1273–1286.

55 Perera, S.A., Gregušová, A., and Bartlett, R.J. (2009). *J. Phys. Chem. A* 113: 3197–3201.

56 Bayar, I., Khedhiri, L., Soudani, S. et al. (2018). *J. Mol. Struct.* 1161: 185–193.

57 Crawford, M.J. and Mayer, P. (2005). *Inorg. Chem.* 44: 8481–8485.

58 Gao, H., Ye, C., Piekarski, C.M., and Shreeve, J.M. (2007). *J. Phys. Chem. C* 111: 10718–10731.

59 Qu, X., Zhang, S., Wang, B. et al. (2016). *Dalton Trans.* 45: 6968–6973.

60 Zhang, Y., Zhang, S., Sun, L. et al. (2017). *Chem. Commun.* 53: 3034–3037.

61 Wang, Y., Zhang, J., Su, H. et al. (2014). *J. Phys. Chem. A* 118: 4575–4581.

62 Sućeska, M. (2013). EXPLO5 6.01[Z]. Brodarski Institute, Croatia.

63 Bushuyev, O.S., Peterson, G.R., Brown, P. et al. (2013). *Chem. Eur. J.* 19: 1706–1711.

64 Li, S., Wang, Y., Qi, C. et al. (2013). *Angew. Chem. Int. Ed.* 52: 14031–14035.

65 Zhang, S., Yang, Q., Liu, X. et al. (2016). *Coord. Chem. Rev.* 307: 292–312.

66 Xu, Y., Lin, Q., Wang, P., and Lu, M. (2018). *Chem. Asian J.* 13: 924–928.

67 Xu, Y., Tian, L., Wang, P. et al. (2019). *Cryst. Growth Des.* 19: 1853–1859.

68 Klapötke, T.M. and Sabaté, C.M. (2010). *Z. Anorg. Allg. Chem.* 636: 163–175.

69 Dippold, A. and Klapötke, T.M. (2012). *Chem. Eur. J.* 18: 16742–16753.

70 Bharatam, P.V., Patel, D.S., and Iqbal, P. (2005). *J. Med. Chem.* 48: 7615–7622.

71 Frisch, M.J., Trucks, G.W., Schlegel, H.B. et al. (2009). *Gaussian 09, Revision A.02*. Wallingford, CT: Gaussian, Inc.

72 (a) Tests were conducted according to the UN Recommendations on the Transport of Dangerous Goods(2009). *Manual of Tests and Criteria*, 5e. New York: United Nations Publication. (b) 13.4.2 Test 3 (a) (ii) BAM Fallhammer, pp. 75–82; (c) 13.5.1 Test 3 (b) (i): BAM friction apparatus, pp. 104–107.

73 Jenkins, H.D.B., Roobottom, H.K., Passmore, J., and Glasser, L. (1999). *Inorg. Chem.* 38: 3609–3620.

74 Zhang, Y., Huang, Y., Parrish, D.A., and Shreeve, J.M. (2011). *J. Mater. Chem.* 21: 6891–6897.

75 Chand, D., Parrish, D.A., and Shreeve, J.M. (2013). *J. Mater. Chem. A* 1: 15383–15389.

76 Sućeska, M. (2013). EXPLO5 6.01. Brodarski Institute, Zagreb, Croatia.